Aerodynamic Design of a Propeller for High-Altitude Balloon Trajectory Control

Richard Eppler and Dan M. Somers

National Aeronautics and
Space Administration

Goddard Space Flight Center
Greenbelt, Maryland 20771

March 2012

NASA STI Program ... in Profile

Since its founding, NASA has been dedicated to the advancement of aeronautics and space science. The NASA scientific and technical information (STI) program plays a key part in helping NASA maintain this important role.

The NASA STI program operates under the auspices of the Agency Chief Information Officer. It collects, organizes, provides for archiving, and disseminates NASA's STI. The NASA STI program provides access to the NASA Aeronautics and Space Database and its public interface, the NASA Technical Report Server, thus providing one of the largest collections of aeronautical and space science STI in the world. Results are published in both non-NASA channels and by NASA in the NASA STI Report Series, which includes the following report types:

- TECHNICAL PUBLICATION. Reports of completed research or a major significant phase of research that present the results of NASA Programs and include extensive data or theoretical analysis. Includes compilations of significant scientific and technical data and information deemed to be of continuing reference value. NASA counterpart of peer-reviewed formal professional papers but has less stringent limitations on manuscript length and extent of graphic presentations.

- TECHNICAL MEMORANDUM. Scientific and technical findings that are preliminary or of specialized interest, e.g., quick release reports, working papers, and bibliographies that contain minimal annotation. Does not contain extensive analysis.

- CONTRACTOR REPORT. Scientific and technical findings by NASA-sponsored contractors and grantees.

- CONFERENCE PUBLICATION. Collected papers from scientific and technical conferences, symposia, seminars, or other meetings sponsored or co-sponsored by NASA.

- SPECIAL PUBLICATION. Scientific, technical, or historical information from NASA programs, projects, and missions, often concerned with subjects having substantial public interest.

- TECHNICAL TRANSLATION. English-language translations of foreign scientific and technical material pertinent to NASA's mission.

Specialized services also include organizing and publishing research results, distributing specialized research announcements and feeds, providing help desk and personal search support, and enabling data exchange services. For more information about the NASA STI program, see the following:

- Access the NASA STI program home page at http://www.sti.nasa.gov

- E-mail your question via the Internet to help@sti.nasa.gov

- Fax your question to the NASA STI Help Desk at 443-757-5803

- Phone the NASA STI Help Desk at 443-757-5802

- Write to:

  NASA STI Help Desk
  NASA Center for AeroSpace Information
  7115 Standard Drive
  Hanover, MD 21076-1320

Aerodynamic Design of a Propeller for High-Altitude Balloon Trajectory Control

Richard Eppler
University of Stuttgart, Stuttgart, Germany

Dan M. Somers
Airfoils, Incorporated, Port Matilda, PA

National Aeronautics and
Space Administration

Goddard Space Flight Center
Greenbelt, Maryland 20771

March 2012

AERODYNAMIC DESIGN OF A PROPELLER FOR HIGH-ALTITUDE BALLOON TRAJECTORY CONTROL

RICHARD EPPLER
UNIVERSITY OF STUTTGART

DAN M. SOMERS
AIRFOILS, INCORPORATED

AUGUST 2005

ABSTRACT

The aerodynamic design of a propeller for the trajectory control of a high-altitude, scientific balloon has been performed using theoretical methods developed especially for such applications. The methods are described. Optimum, nonlinear chord and twist distributions have been developed in conjunction with the design of a family of airfoils, the SE403, SE404, and SE405, for the propeller. The very low Reynolds numbers along the propeller blade fall in a range that has yet to be rigorously investigated, either experimentally or theoretically.

INTRODUCTION

Scientific balloons, including future Ultra Long Duration Balloons (ULDB), require a system for the control of flight trajectory. One such trajectory-control system employs a propeller. The design of the propeller represents a challenge, however, because of the very low Reynolds numbers (< 50,000) characteristic of the high operational altitudes. Accordingly, the aerodynamic design of the propeller has been performed using theoretical methods developed especially for such applications. The propeller design includes not only the optimum planform of the blades (i.e., chord and twist distributions) but also the airfoil shapes along the radius of the blade.

Propeller theory, as it has commonly been applied to date, is based on a method developed in 1919 (refs. 1 and 2). This theory assumes a low, propeller loading and neglects viscous drag. It has been successfully applied to many lowly loaded propeller designs, including those for man-powered and solar-powered aircraft. A theory for more highly loaded, optimum propellers, still ignoring viscous drag, was developed recently ("Propellers and Fans," seminar by R. Eppler at Siegen University, Germany, 15 April 1999). One result from the application of this theory is that the lift is shifted considerably outboard if the propeller is more highly loaded, which is understandable because the lift outboard produces less torque. Lately, it has been concluded empirically that viscous drag too influences the optimum lift distribution along the propeller blade because overcoming the drag outboard requires much more power than inboard.

The design of an optimum, solar-powered propeller for a high-altitude balloon can not be performed adequately without accounting for the viscous drag because the Reynolds numbers are so low. Accordingly, the recent theory has been extended to include viscous drag. The first application of the extended theory is presented. The effect of the viscous drag is much greater than previously suspected. The lift is shifted back inboard but in a different way than it is shifted outboard in the case of high loading.

Because the airfoil performance is the key to the propeller performance and because current theoretical airfoil methods (e.g., refs. 3–5) have not been validated for such low Reynolds numbers, it is imperative that an appropriate airfoil from the propeller design (e.g., 75-percent radius) be experimentally verified.

SYMBOLS

B	number of blades
C_p	power coefficient; pressure coefficient
C_T	thrust coefficient
c	chord, m
c_d	section profile-drag coefficient
c_l	section lift coefficient
c_m	section pitching-moment coefficient about quarter-chord point
D	drag, N
H	function
L	lift, N
M	Mach number
P	shaft power, W
p	static pressure, Pa
R	radius to blade element, m; Reynolds number based on free-stream conditions and chord
r	nondimensional radius to blade element, $\dfrac{R}{R_t}$
T	thrust, N
t	airfoil thickness, m
t_{infl}	time after which influence of vortex elements on blade forces is neglected, s
t_{max}	maximum lifetime of vortex elements, s
U	induced velocity parallel to rotational direction, m/s; blade rotational velocity, ωR, m/s
u	nondimensional induced velocity parallel to rotational direction, $\dfrac{U}{\omega R_t}$

V_∞	forward velocity of propeller, m/s
W	induced velocity parallel to propeller axis, m/s
w	nondimensional induced velocity parallel to propeller axis, $\dfrac{W}{\omega R_t}$
x	airfoil abscissa, m
y	blade abscissa, perpendicular to propeller axis and propeller radius, m; airfoil ordinate, m
z	blade ordinate, parallel to propeller axis, m
α	angle of attack relative to x-axis, deg
Γ	circulation, m^2/s
γ	velocity jump across vorticity layer, ΔU, m/s; lift distribution
Δ	incremental change in quantity
δ	$= \text{atan}\dfrac{D}{L}$
ε	$= \dfrac{D}{L}$
η	efficiency
θ	rotational angle, deg
Λ	Lagrange multiplier
λ	nondimensional forward velocity of propeller, $\dfrac{V_\infty}{\omega R_t}$
ρ	air density, kg/m^3
Φ	Lagrange function
ϕ	angle between local flow velocity and rotational direction, deg; twist angle, deg
Ψ	function for u and w
ω	angular velocity, rad/s
∞	infinity

Subscripts:

Betz   Betz solution (see ref. 1)

L   at blade

max   maximum

min   minimum

mn   near minimum

n   normalized

S   separation

t   tip

0   far upstream of propeller; index of function H for $u = 0$ and $w = 0$; zero lift

1   upstream of cylinder; at propeller; index of partial function Φ

2   downstream of cylinder; far downstream of propeller; index of partial function Φ

∞   free-stream conditions

Abbreviations:

L.   lower surface

S.   boundary-layer separation location, x_S/c

U.   upper surface

<div align="center">

PLANFORM

THEORY

Blade-Element Theory
</div>

The blade elements of the propeller are located on concentric cylinders around the propeller axis at a radius R and have a radial length of dR. One such cylinder, unrolled into a plane, is shown in figure 1. The pressure upstream of the cylinder is p_1 and downstream, p_2.

The velocities induced by the propeller are U_1 and W_1 upstream of the cylinder, U_2 and W_2 downstream, and U_L and W_L at the propeller blade. The velocity at a blade section is composed of the downstream velocity $V_\infty + W_L$ and the rotational velocity $\omega R - U_L$, where V_∞ is the forward velocity of the propeller (i.e., the velocity of advance) and ω is the angular velocity of the blade. The velocities U_1, W_1, U_2, and W_2 and the pressure difference $\Delta p = p_2 - p_1$ depend on the radius R of the cylinder and the rotational angle θ. The propeller has B blades. The direction of the local velocity is determined by the angle ϕ for which

$$\tan\phi = \frac{V_\infty + W_L}{\omega R - U_L} \tag{1}$$

The lift L of the section is perpendicular to the local velocity and the drag D is perpendicular to the lift. The resulting force forms an angle to the lift vector defined by $\tan\delta = D/L = \varepsilon$.

Blade-element theory works with averaged velocities such as

$$\overline{U_1}(R) = \frac{1}{2\pi} \int_0^{2\pi} U_1(R, \theta)d\theta$$

and the corresponding averaged pressure differences $\overline{\Delta p}(R)$. This introduces several difficulties. For example, for continuity reasons, $\overline{W_1}$ must equal $\overline{W_2}$. This is not true for W_1^2 and W_2^2, which are difficult to evaluate. Also, the contraction of the propeller jet over the finite height of the cylinder is neglected.

The only simple and clear averaging that can be performed is to replace the finite number of propeller blades by an infinite number of infinitesimal blades, as illustrated in figure 2. On the left side of figure 2, several small vortices are shown along with their directions of rotation. If weaker and weaker vortices are supposed, they approach a vorticity surface, which is represented on the right side of figure 2 by a broken line that moves to the right with the velocity ωR. Such a vorticity layer is merely a discontinuity in the velocity field. The velocity jumps across the vorticity layer by $\Delta U = \gamma$, which is the strength of the vorticity layer. The direction of ΔU is perpendicular to the direction of the vector $\vec{\gamma}$, which, in the present case, is the radial direction. The height of the previously considered cylinder becomes infinitesimal and the induced velocities become

$$U_2 - U_1 = \gamma \qquad\qquad U_L = (U_1 + U_2)/2 \qquad\qquad W_1 = W_2 = W_L$$

If the flow upstream of the propeller is irrotational, $U_1 = 0$. Then, as shown in figure 2,

$$W_1 = W_2 = W_L = W \qquad\qquad U_2 = U = \gamma \qquad\qquad U_L = U/2$$

can be set. Upstream of the propeller, the Bernoulli equation

$$p_\infty + \frac{\rho}{2}V_\infty^2 = p_1 + \frac{\rho}{2}(V_\infty + W)^2 \tag{2}$$

is valid. Downstream of the propeller, the jet rotates, contracts, and becomes turbulent. It is assumed that the Bernoulli equation along the streamlines is valid until the pressure has reached free-stream static p_∞. Thus,

$$p_2 + \frac{\rho}{2}((V_\infty + W)^2 + U^2) = p_\infty + \frac{\rho}{2}((V_\infty + W_\infty)^2 + U_\infty^2) \tag{3}$$

where $U_\infty = U$ due to the conservation of momentum. Thus, the pressure difference across the propeller disk is

$$\Delta p = p_2 - p_1 = \frac{\rho}{2}(2V_\infty W_\infty + W_\infty^2) \tag{4}$$

An infinitesimal blade element of the rotating propeller extends over a sector of the propeller disk having the angle $d\theta$. The circulation on that blade element is $\gamma(R)Rd\theta$. The direction of the flow at this element is given by

$$\tan\phi = \frac{V_\infty + W}{\omega R - U/2} \tag{5}$$

The lift on this blade element is perpendicular to the direction of the flow and its magnitude is

$$ddL = \rho\gamma RdRd\theta\sqrt{(\omega R - U/2)^2 + (V_\infty + W)^2} = \rho\gamma RdRd\theta\frac{\omega R - U/2}{\cos\phi} \tag{6}$$

The corresponding thrust element is

$$ddT = \frac{ddL}{\cos\delta}\cos(\phi + \delta)$$

and the thrust element for the entire "ring" is, with $\gamma = U$,

$$dT = 2\pi\rho URdR\frac{\omega R - U/2}{\cos\phi}(\cos\phi - \tan\delta\sin\phi)$$

or, using equation (5) and $\tan\delta = \varepsilon$,

$$dT = 2\pi\rho U(\omega R - U/2 - \varepsilon(V_\infty + W))RdR \tag{7}$$

The same thrust element results from the pressure difference Δp, which yields, using equation (4),

$$dT = \Delta p 2\pi RdR = \pi\rho(2V_\infty W_\infty + W_\infty^2)RdR \tag{8}$$

Another formula follows from the total flow through the ring. The flow is contained in a tube having variable radius R and radial length dR. Its cross section is shown in figure 3. The radius far upstream of the propeller is R_0; far downstream, R_2; and at the propeller, R_1. The corresponding widths of the tube are dR_0, dR_1, and dR_2, which are determined by the continuity condition

$$R_0 dR_0 V_\infty = R_1 dR_1(V_\infty + W) = R_2 dR_2(V_\infty + W_\infty) \tag{9}$$

where the factor 2π has been omitted. The pressure integral around this tube vanishes due to the properties of the flow about an infinite half body. The external force $\Delta p 2\pi R_1 dR_1$ acts at the propeller disk. The momentum equation in the direction of the propeller axis yields then

$$\rho V_\infty^2 R_0 dR_0 + \Delta p R_1 dR_1 - \rho(V_\infty + W_\infty)^2 R_2 dR_2 = 0$$

again without the factor 2π. Together with equation (9), it follows that

$$\Delta p = \rho(V_\infty + W)W_\infty$$

Comparing this equation with equation (4) yields immediately

$$W_\infty = 2W$$

This simple equation results in momentum theory as well. Half the downstream velocity produced by the propeller is already present at the propeller. With this equation, it follows from equation (8) that

$$dT = 4\pi\rho(V_\infty W + W^2)R dR$$

and, by comparing this equation with equation (7),

$$2W(V_\infty + W) = U(\omega R - U/2 - \varepsilon(V_\infty + W)) \tag{10}$$

The total thrust can thus be evaluated by two formulas

$$T = 4\pi\rho \int_0^{R_t} W(V_\infty + W)R dR \tag{11}$$

$$T = 2\pi\rho \int_0^{R_t} U(\omega R - U/2 - \varepsilon(V_\infty + W))R dR \tag{12}$$

where R_t is the radius of the propeller. The power required to move a ring element is

$$ddP = \frac{ddL}{\cos\delta}\sin(\phi + \delta)\omega R$$

with ddL from equation (6). This yields the total power required

$$P = 2\pi\rho\omega \int_0^{R_t} U(V_\infty + W + \varepsilon(\omega R - U/2))R^2 dR \tag{13}$$

Nondimensional Variables

To nondimensionalize the variables, all lengths are divided by the propeller radius R_t and all velocities, by the rotational velocity at the propeller tip $U_t (= \omega R_t)$. The pressures are

divided by ρU_t^2 and the forces, by $\rho U_t^2 R_t^2$. In this report, to the extent possible, the dimensional variables are designated by upper-case letters and the nondimensional variables, by the corresponding lower-case letters. For example,

$$u = \frac{U}{\omega R_t} \qquad\qquad w = \frac{W}{\omega R_t} \qquad\qquad r = \frac{R}{R_t}$$

The nondimensional forward velocity of the propeller is

$$\lambda = \frac{V_\infty}{\omega R_t}$$

which is proportional to the advance ratio.

The nondimensionalized ωR is merely r. Accordingly, equation (5) becomes

$$\tan\phi = \frac{V_\infty + W}{\omega R - U/2} = \frac{\lambda + w}{r - u/2} \tag{14}$$

and equation (10),

$$\Psi(u, w) = 2w(\lambda + w) - u(r - u/2 - \varepsilon(\lambda + w)) = 0 \tag{15}$$

The thrust T and the power required P are given in terms of their corresponding coefficients

$$C_T = \frac{T}{2\pi\rho R_t^2(\omega R_t)^2} = \frac{T}{2\pi\rho R_t^2 U_t^2} = \int_0^1 2w(\lambda + w)r\,dr \tag{16}$$

$$C_P = \frac{P}{2\pi\rho\omega R_t^3(\omega R_t)^2} = \frac{P}{2\pi\rho R_t^2 U_t^3} = \int_0^1 u(\lambda + w + \varepsilon(r - u/2))r^2\,dr \tag{17}$$

Optimum Propeller Design

Formulation of problem.- The thrust and power coefficients depend, according to equations (16) and (17), on the given parameters λ and ε, r, and the functions $w(r)$ and $u(r)$. The two functions are not independent, however. Using equation (15), one function can be evaluated if the other is known. Therefore, only one of the functions is free. This means that C_T and C_P depend on one of these functions.

The requirements for an optimum propeller can be specified in different ways.

(1) Minimum power for a given thrust

(2) Maximum thrust for a given power

(3) Maximum thrust-to-power ratio

8

The only function that is free for achieving the optimum is either $u(r)$ or $w(r)$. Such optimization problems are typical for variational calculus.

From the different formulations of the variational problem, the following has been selected: for the specified thrust T, the power required P must be minimum. The free function is $w(r)$; $u(r) = u(w(r))$ is given, with $w(r)$ according to equation (15). Mathematically, this is formulated with a Lagrange multiplier Λ. The Lagrange function

$$\Phi(w(r)) = \int_0^1 (\Phi_1(w) - \Lambda\Phi_2(w))dr \tag{18}$$

is defined with

$$\Phi_1(w) = u(\lambda + w + \varepsilon(r - u/2))r^2 \tag{19}$$

$$\Phi_2(w) = 2w(\lambda + w)r \tag{20}$$

and equation (15). The necessary condition for the defined optimum is

$$\frac{d}{dw}(\Phi_1 - \Lambda\Phi_2) = 0 \tag{21}$$

where Φ_1 depends on w and $u(w)$ and, therefore,

$$\frac{d\Phi_1}{dw} = \frac{\partial\Phi_1}{\partial w} + \frac{\partial\Phi_1}{\partial u}\frac{du}{dw} \tag{22}$$

where

$$\frac{du}{dw} = -\frac{\dfrac{\partial\Psi}{\partial w}}{\dfrac{\partial\Psi}{\partial u}}$$

Using $\Psi(u,w)$ from equation (15),

$$\frac{du}{dw} = \frac{2\lambda + 4w + \varepsilon u}{r - u - \varepsilon(\lambda + w)} \tag{23}$$

The central optimization condition represented by equation (21) is a simple, special case of the Euler equation of the variational problem because dw/dr does not occur in equation (18). Equation (21) concerns only the integrand of equation (18) and must be satisfied for each r.

Properties of function $u(w)$.- Equation (15) is quadratic in u and w. Because both terms containing u^2 and w^2 have the same sign, an ellipse is represented for each r. It is possible to solve equation (15) with respect to u by

$$u = r - \varepsilon(\lambda + w) - \sqrt{(r - \varepsilon(\lambda + w))^2 - 4w(\lambda + w)}$$

9

Only the negative sign of the square root is realistic because the positive sign would yield u values greater than r. All solutions go through $u = w = 0$. A series of the resulting ellipses is shown in figure 4; the largest, for $r = 1$, and the others, for monotonically smaller r values.

The maximum $w\ (= w_{max})$ for which a u is defined makes the argument of the square root zero. This yields

$$w_{max} = -\frac{2\lambda + \varepsilon(r - \varepsilon\lambda)}{4 - \varepsilon^2} + \sqrt{\left(\frac{2\lambda + \varepsilon(r - \varepsilon\lambda)}{4 - \varepsilon^2}\right)^2 + \frac{(r - \varepsilon\lambda)^2}{4 - \varepsilon^2}} \tag{24}$$

It follows that the maximum $u\ (= u_{max})$ is

$$u_{max} = r - \varepsilon(\lambda + w_{max}) \tag{25}$$

Obviously, there is also a minimum r, below which equation (15) has no solution. For $r = \varepsilon\lambda$, it follows from equations (24) and (25) immediately that

$$w_{max} = u_{max} = 0$$

In equation (23), the denominator is zero for $u = u_{max}$ and $w = w_{max}$; there, the ellipses have their vertical tangents. More difficult is the other singularity at $r = \varepsilon\lambda$. For w and $u \to 0$, it follows that $du/dw \to -\infty$.

Optimization details.- The Lagrange multiplier Λ in equation (21) is normally determined such that the specified C_T is achieved. To obtain an overview of the possible solutions, it is simpler to vary Λ, however. Therefore, the range of Λ values that leads to solutions must be determined. From equation (19), it follows that

$$\frac{d\Phi_1}{dw} = \left(u + (\lambda + w + \varepsilon r - \varepsilon u)\frac{du}{dw}\right)r^2$$

and, from equation (20),

$$\frac{d\Phi_2}{dw} = (2\lambda + 4w)r$$

Both equations, when introduced into equation (21), yield the optimum condition

$$\left(u + (\lambda + w + \varepsilon r - \varepsilon u)\frac{du}{dw}\right)r^2 - \Lambda(2\lambda + 4w)r = 0 \tag{26}$$

which must be satisfied for all values of r considered. All variables u, w, ε, and r must be greater than zero. Moreover, only u less than r makes sense. The opposite would mean that the induced velocity U is greater than ωR and, thus, the induced velocity would be greater than the rotational velocity. Accordingly, the term within the inner parentheses of the first term in equation (26) is not negative and can be zero only for $u = w = \varepsilon = 0$. The first term becomes $+\infty$ as $w \to w_{max}$. For any r, a solution exists once there is a w for which the left side of equation (26) is negative.

It has been shown that below $r_{min} = \varepsilon\lambda$, no solution can exist. Moreover, for $r = r_{min}$,

$$\frac{du}{dw} = -\frac{\varepsilon u + 2\lambda + 4w}{u + \varepsilon w}$$

tends toward $-\infty$ for u and $w \rightarrow 0$. The first term in equation (26) thus has very large values for $r \rightarrow r_{min}$. For these r values, solutions can exist only for very large Λ values. It is, therefore, necessary to study the possible solutions in more detail. Once an arbitrary w can be found for a given r and Λ, for which the function

$$H(u(w), w, r) = \frac{\left(u + (\lambda + w + \varepsilon r - \varepsilon u)\dfrac{du}{dw}\right)r}{2\lambda + 4w} < \Lambda$$

then a solution w exists because also $H \rightarrow \infty$ for $w \rightarrow w_{max}(r)$, according to equation (24). In figure 5, $H(w)$ is shown for $\lambda = 0.2$ and $\varepsilon = 0.05$ and a series of r values. From this figure (and a common property of H), it can be concluded that H always increases with w. A unique solution is, therefore, guaranteed once

$$H_0 = H(r, u = 0, w = 0) = \frac{(\lambda + \varepsilon r)r\dfrac{2\lambda}{r - \varepsilon\lambda}}{2\lambda} = \frac{(\lambda + \varepsilon r)r}{r - \varepsilon\lambda} < \Lambda$$

Also shown in figure 5 is a diagram of $H_0(r)$ for $\lambda = 0.2$ and six values of ε. All curves are hyperbolas with a vertical asymptote at $r = \varepsilon\lambda$ and the second asymptote according to

$$H_0 = \lambda(1 + \varepsilon^2) + \varepsilon r$$

The Lagrange multiplier Λ is the same for all r. If

$$\Lambda = H_0(1) = \frac{\varepsilon + \lambda}{1 - \varepsilon\lambda}$$

solutions exist, according to the function $H_0(r)$ shown in figure 5, for all r down to the small r_{mn} for which

$$H_0(r_{mn}) = H_0(1)$$

This limit is represented in figure 5, for $\varepsilon = 0.01$ and $\varepsilon = 0.06$, by broken lines connecting the points $H_0(1)$ and $H_0(r_{mn})$.

For $\Lambda > H_0(1)$, this range can be slightly extended. In this case, the lower limit of the solution range is

$$r_{mn} = \frac{\Lambda - \lambda}{2\varepsilon} - \sqrt{\left(\frac{\Lambda - \lambda}{2\varepsilon}\right)^2 - \lambda\Lambda}$$

The range for which no solution exists is very small and, in practical applications, is covered by the hub.

If a specified C_T is to be achieved, the algorithm is slightly different. Instead of selecting Λ values, Λ must be determined iteratively such that the desired C_T is achieved.

Finite number of blades.- As in all "averaged" propeller theories, the discretization of the infinite number of blades into B blades must be performed by concentrating the Bth part of the vorticity surface onto one blade. The total circulation of this blade is

$$\Gamma = \gamma R \frac{2\pi}{B}$$

The lift due to this circulation on a blade element of length dR results from equation (6) if $d\theta$ is replaced by $2\pi/B$

$$dL = \rho\gamma\frac{2\pi}{B}\sqrt{(V_\infty + W)^2 + (\omega R - U/2)^2}\,R\,dR = c_l\frac{1}{2}\rho((V_\infty + W)^2 + (\omega R - U/2)^2)c\,dR$$

where $c(R)$ is the local chord of the blade. This yields, with $\gamma = U$,

$$c_l c = \frac{4\pi U R}{B\sqrt{(V_\infty + W)^2 + (\omega R - U/2)^2}}$$

or, nondimensionalized,

$$c_l\frac{c}{R_t} = \frac{4\pi u r}{B\sqrt{(\lambda + w)^2 + (r - u/2)^2}} \tag{27}$$

This equation determines the chord distribution $c(r)$ once the lift coefficient of the blade element is known.

The twist of the blade is determined by the angle ϕ. It shows the (average) direction of the local flow. Relative to this direction, the airfoil must have the angle of attack needed to generate the lift coefficient that was used to determine the chord according to equation (27). If the chord is large, the velocities induced by the wake may change along the chord. The induced velocities along the chord should then be calculated using another method (e.g., ref. 6).

RESULTS

Inviscid Solutions

The inviscid case is obtained by setting ε to zero in all the formulas. For two values of λ, 0.026 and 0.2, only Λ was varied; C_T and ur depend on Λ. For easier comparison with the Betz solution, ur is shown in figure 6 normalized by dividing all ur values by $C_T/C_{T,Betz}$. Thus, the ordinate is

$$(ur)_n = ur\frac{C_{T,Betz}}{C_T}$$

The solid lines represent the results of the present theory. The broken line represents the result from the theory of Betz (ref. 1). The first and last values of C_T are written next to the first and last solid lines.

Several results are significant.

(1) The present theory converges to the Betz solution as $C_T \to 0$.

(2) For the lower λ (= 0.026), relatively low values of C_T already yield curves that deviate considerably from the Betz solution. The curve for $C_T = 0.009$ is the seventh one from the Betz solution.

(3) For the higher λ (= 0.2), the deviation from the Betz solution is smaller although still not negligible.

Optimum propellers for finite loadings have lift distributions shifted toward the blade tip compared to the classical solution. The highest C_T shown in figure 6 yields very large chords, typical of ship propellers.

Effect of Viscosity

The viscosity is embodied by the parameter ε, which is the drag-to-lift ratio of the airfoil. The design of propellers for low Reynolds numbers must generally consider ε values greater than 0.03. Propellers having rough leading edges may also have an ε value of 0.015 at higher Reynolds numbers. The following examples are representative of a two-bladed propeller for a balloon operating at very high altitudes (see table I). At the specified altitude, the very low air density leads to Reynolds numbers around 12,000, despite the required large chords. Therefore, ε values up to 0.05 have been evaluated. The thrust coefficient C_T and the nondimensional forward velocity λ are given in each example.

In figure 7, λ corresponds to the specified, low velocity of the balloon. The optimum propeller, including viscous effects, has reduced lift near the blade tip and increased lift inboard of about 75-percent radius. The difference from the inviscid solution is not dramatic but also not negligible.

The effects of a higher λ value and different C_T values are shown in figure 8. For the lower C_T value, the effect of viscosity is even greater than for the low λ value. Increasing C_T decreases the effect.

Optimum Propellers

If no parameters are varied, not only $c_l c/R_t$ but also the twist angle ϕ and the Reynolds number R are plotted, as shown in figure 9 for the two-bladed propeller at the specified forward speed.

The given tip speed U_t is a driving parameter. The results are:

(1) The power required for all three tip speeds is within the specified limit.

(2) The power required decreases with decreasing tip speed.

(3) The local blade chords increase with decreasing tip speed.

(4) The Reynolds numbers increase with decreasing tip speed.

The planform of the propeller with the lowest power required (fig. 9(a)) exhibits large chords inboard (e.g., for $c_l = 1$, $c > 2$ m). The incorporation of these large chords inboard requires careful consideration. In this region, the blade design is determined by structural requirements, as is typical. Also, although the Reynolds number is extremely low, because this region contributes little to the total thrust and power required, no aerodynamic concerns arise.

Propeller Analysis

The optimum propellers have been developed using a propeller theory that does not consider the velocities induced by the vortices in the jet downstream of the propeller. The most and the strongest vortices are shed from the trailing edge of the propeller blades near the tips. By neglecting these vortices, a ducted fan is considered rather than a free propeller. This is also true for the fundamental method of reference 1, which was corrected by the supplement in the same reference. The corrected method is widely used today (e.g., ref. 2) and has been employed to modify the tip of the optimum propeller blade. Accordingly, the method of reference 6, referred to as the Zerle code in this report, has been used to investigate the development of the vortex wake produced by the propeller.

Vortex lattice and vorticity layer.- The wake downstream of a wing or propeller blade is a layer of vorticity having finite thickness. It would best be described by the Navier-Stokes equations. A viscous, computational fluid dynamics (CFD) code has yet to accurately treat the vortex wake downstream of a propeller or helicopter rotor, however. Alternatively, several methods employ an inviscid idealization in which the vorticity layer of the wake is represented by a two-dimensional, vortex surface. The movement of this vortex surface is, however, difficult to compute. Accordingly, the vortex surface is usually discretized by a vortex lattice, as in the Zerle code.

The representation of the vortex surface by a vortex lattice has several shortcomings.

(1) Mathematically, a single vortex is represented by a potential flow, which is irrotational. The (possibly curved) axis of the vortex represents a strong singularity in this flow. For example, a vortex of finite strength contains an infinite amount of energy. This singularity is normally eliminated by assuming a vortex core of finite diameter, where the velocity tends toward zero instead of infinity. Only outside this core is the flow irrotational. The radius of the core influences the results, however.

14

(2) A mathematical vortex with no core induces a velocity at any point outside the vortex according to the well-known Biot-Savart formula. The term "induced velocity" is somewhat misleading, however. This velocity must exist if the flow outside the vortex is irrotational and, therefore, a potential flow. If the vortex is a straight line of infinite length, the Biot-Savart formula yields the simple, two-dimensional, vortex flow, in which the streamlines are circles around the vortex axis and the velocity is inversely proportional to the radius of the circle.

(3) A curved vortex induces an infinite velocity at any point on itself. The vortex would then move with this velocity. This is again prevented by the vortex core but the numerical results may vary greatly with core radius.

(4) If a nonsingular potential flow is superposed on a vortex flow, a force acts on each element of the vortex proportional to the strength of the vortex and the local velocity of the superposed flow. This force is also infinite for a curved vortex with no core.

(5) The vortex surface (or layer) downstream of a wing or propeller blade rolls up aft of the tips and, thereby, no part of the vortex surface can penetrate any other part of the vortex surface. The cross sections through the wake become spirals. The vortices of the vortex lattice also exhibit the typical roll up but they penetrate the vortex lattice representing the vortex surface. This leads to a chaotic mixing of the vortices that does not model the roll up of the vortex surface. Moreover, the roll up of the vortex lattice begins earlier and much faster than the roll up of the vortex surface.

All these shortcomings raise the question whether reliable results can be obtained from a vortex-lattice method. Many valuable results have been presented, however, for fixed geometries and fixed wakes without relaxation. In this case, the induced velocities are only considered at the center of the doublet elements, which never coincide with a flow singularity. If the velocity normal to the blade surface is required to be zero at these points, the total "leakage" through the vortex lattice is small because the positive and negative contributions tend to cancel each other. This is still true if a vortex wake is assumed to have a fixed form. Once the wake is to be adapted to the local induced velocities, however, the shortcomings become almost overwhelming.

Zerle code.- To determine the differences between the results from blade-element theory and the propeller with a free wake, it is most important to know the induced velocities from the wake onto the propeller blade. These velocities depend on the shape of the wake. It is known that the jet behind a propeller contracts and increases its downstream velocity. If the propeller moves in the direction of its axis, the vorticity vector always has the direction of the local velocity vector.

The shape of the wake is thus determined by the velocity field downstream of the propeller. This velocity field is composed of the velocities due to the movement of the propeller and the induced velocities from the propeller and the wake. No velocity component perpendicular to the surface of the vortex wake is permitted. The solution of this problem normally requires an iterative approach because the velocity field depends on the lift of the propeller

blades and the shape of the wake whereas the lift of the blades and, therefore, the vorticity strength of the wake depend on the induced velocities.

The Zerle code starts with the given shape of the blade, although the blade sections have no thickness. The blade and the wake are represented by panels having constant doublet strength and straight edges, which correspond to vortex rings.

Instead of the iterative method previously discussed, the Zerle code starts from the propeller with no wake and then develops the wake in time steps. After each time step, the wake is updated. The wake elements from the preceding time step move with the local velocities and a new row of wake elements is introduced at the trailing edge of the blade. The new elements contain only longitudinal vortices if the circulation at the radius has not changed. If the circulation has changed, the elements also contain lateral vortices.

In calculating the strength of the doublet panels of the blade, all induced velocities from the wake and the blade panels are considered. All vortices represent singularities in the flow because the induced velocity of a vortex element tends toward infinity with decreasing distance from the vortex element. This is, as previously mentioned, no problem for fixed blade geometries and fixed wakes. For a free wake, however, the distance between the vortices may become very small or even zero. For these vortices, a so-called damping radius is therefore introduced, within which the induced velocity tends toward zero instead of infinity. This does not, however, prevent the chaos that occurs if vortices penetrate the vortex lattice, unless the damping radius is very large. In this case, the essential effects of the wake movement are lost. For calculating the displacement of the wake elements, a small damping radius is also used for the blade vortices.

The greatest difficulty for vortex-lattice methods, including the Zerle code, is the computation of the free wake. The shape of the vortex lattice, in which all vortex elements influence the movement of each other, is much more unstable than the shape of a vorticity surface, which, in turn, is much more unstable than a vorticity layer of finite thickness. Frequently, the movement of the vortex lattice becomes chaotic and is no longer representative of the real wake. The instability is greatest at the beginning of the wake development. After less than one revolution of the propeller, the wake can become completely chaotic. The chaotic portion of the wake moves downstream, however, and the wake being shed from the trailing edge is less unstable. The forces on the propeller often converge to asymptotic values. The induced velocities from the wake onto the blades decrease rapidly with distance from the propeller. Accordingly, a maximum lifetime t_{max} of the vortex elements has been introduced, after which their induced velocities are neglected. In other words, an artificial termination of the wake has been introduced. To avoid errors near the artificial terminus, t_{max} must be large enough that the evaluation of the forces on the propeller will result in very little error when elements having a lifetime greater than $t_{infl} (< t_{max})$ are neglected. The most important criterion for the validity of the results is the convergence of the forces on the propeller to asymptotic values with increasing time.

Modifications to Zerle code.- The number of panels in the Zerle code is limited to 6 chordwise and 20 spanwise, which is insufficient for the current problem. Therefore, the

number of panels has been increased to 16 chordwise and 32 spanwise. Moreover, nondimensional variables have been introduced in the same way as previously described. Simultaneously, the code was converted to double precision from single precision because of the increased number of panels and, correspondingly, the size of the linear equation systems.

The major difficulty of the Zerle code is the unstable shape of the vortex lattice of the wake. The instability is increased by the finer panelling. In two regions, the instability is very persistent: the center of the wake and the roll up at the outer edge of the wake.

The following modifications to the Zerle code improve the behavior of the wake such that, in most cases, an asymptotic convergence is achieved.

(1) The amount of rotation between two vortex elements is limited, which is effective primarily near the outer edge of the wake where it retards the roll up.

(2) During the development of the wake, the lift on the blade varies. The resulting lateral vortices in the wake increase the instability of the wake near the propeller axis. This is reduced by neglecting the shedding of lateral wake vortices for varying lift. This does not introduce an error in the asymptotic case, where the lift is constant.

(3) A maximum lifetime t_{max} of the vortex elements of the wake (typically, equivalent to four revolutions) is introduced, after which all induced velocities from the elements are neglected. The wake, which extends downstream to infinity, is artificially terminated at t_{max}.

(4) An influence time t_{infl} $(< t_{max})$ is introduced, after which the induced velocities from the elements onto the blades are neglected.

(5) The total time for which the development of the wake is computed is always greater than t_{max}. A considerable portion of the wake has then departed the computation domain. A total time corresponding to six propeller revolutions is usually sufficient.

Results of analysis.- The two-bladed propeller exhibiting the highest performance (fig. 9(a)) has been evaluated using the modified Zerle code. The tip speed U_t is 50 m/s and the radius R_t is 5 m. The modification of the tip according to reference 2 increases the radius to 5.2 m and the tip speed to 52 m/s. A circular arc was used for the airfoil shape. An angle of attack of 3 degrees is necessary for this airfoil shape to reach the desired lift coefficient of 1. The chord of the propeller blade has been reduced slightly near the axis. This region will be determined by structural requirements, in any event. The propeller and the computational panels are shown in figure 10 as an axonometric projection and a plan view.

The development of the wake is shown in figure 11 after one through six revolutions; 24 time steps per revolution have been computed. (Note that the wakes have been terminated at t_{infl}, equivalent to three revolutions in this case.) The projection direction is the longitudinal axis of the propeller, which shows primarily the profiles of the propeller. It should be noted that the airfoils are laid out on cylinders and appear, in this projection, not in their exact shapes. After one revolution, the wake seems to develop regularly, although its downstream velocity is too low and some irregularities occur in the center of the wake. After two revolu-

tions, the downstream velocity of the wake has increased and the irregularities in the center of the wake have grown into a chaotic region. After three revolutions, the chaotic region has increased in extent and moved downstream. After four revolutions, a portion of the chaotic region has already exceeded the time range of three revolutions shown. It has not yet, however, exceeded the range where it influences the shape of the wake. This is also true after five and six revolutions, where the wake gradually becomes regular.

After each time step, the forces and moments are evaluated. During the final revolution, the thrust varies between 21.0 N and 21.3 N, which is near the design requirement.

All the results from the inviscid and viscous theories have been compared to those from the simple formulas of the momentum or jet theory of propellers (e.g., refs. 7 and 8). The very low nondimensional forward velocity (i.e., advance ratio) of the present propeller is close to the static case, in which the power P and the thrust T of the propeller are related by the formula

$$T^3 = 2\pi\rho R_t^2 P^2$$

The thrust from the momentum theory cannot be realized because this theory neglects the rotational energy of the propeller jet. Accordingly, an efficiency η is introduced into the above formula

$$T = \eta \sqrt[3]{2\pi\rho R_t^2 P^2}$$

For all results from the inviscid theory, η is slightly less than 1, which demonstrates that the details of the vortex wake influence the efficiency very little.

The viscous theory yields $\eta = 0.753$. Values of $\eta \approx 0.7$ are typical of propellers that are not designed for the static case. Thus, the value for the present propeller appears to be reasonable.

The local induced velocities from the wake onto the propeller blade can also be evaluated from the asymptotic wake. Qualitatively, they do not differ greatly from the values computed by the present method. The thrust agrees well and both methods exhibit higher downstream velocities toward the center of the wake.

A decambering effect on the airfoil may be present because the aspect ratio of the blade is low and the induced velocities from the wake are lower at the leading edge than at the trailing edge of the blade. The airfoil must then have more camber than in the infinite, straight flow assumed in theoretical and experimental airfoil evaluations.

Because of the very low Reynolds numbers, the uncertainties in the section characteristics of the airfoil are at least of the same order of magnitude as the uncertainties in the propeller theories. The final propeller shape can be determined once the aerodynamic performance of the airfoil is known.

AIRFOILS

DESIGN

Objectives and Constraints

The airfoil design specifications, which are derived from the propeller performance requirements, are contained in table II. Two primary objectives are evident. The first objective is to achieve a high lift-to-drag ratio for a Reynolds number of 10,000. The second objective is to provide a reasonable range of lift coefficients over which no significant separation occurs for the same Reynolds number. This range is intended to provide a margin against such contingencies as manufacturing tolerances, operational deviations, three-dimensional effects, and inaccuracies in the theoretical methods. Note that, because the free-stream Mach number for all relevant operating conditions remains below 0.2, the flow is considered incompressible (i.e., $M = 0$).

Two major constraints were placed on the airfoil design. First, the zero-lift pitching-moment coefficient must be no more negative than –0.20. Second, the airfoil thickness must be at least 3-percent chord for structural reasons.

In addition to the airfoil specified by these requirements, designated the primary airfoil, two thicker airfoils are desirable for the root region of the blade because of structural considerations.

Philosophy

Given the above objectives and constraints, certain characteristics of the design are apparent. To achieve a high lift-to-drag ratio (i.e., a low ε), it is more efficacious to pursue higher lift coefficients than lower profile-drag coefficients, especially because the very low Reynolds numbers will likely result in laminar flow over the entire airfoil. Thus, at the maximum lift coefficient, the entire upper surface should be used for the pressure recovery. The same is true for the lower surface at the minimum lift coefficient. To achieve a reasonable range of lift coefficients without significant separation, the airfoil thickness should be increased, although the thickness is constrained by the goal of higher lift coefficients.

From the preceding discussion, the pressure distributions along the drag polar can be deduced. The pressure distribution near the maximum lift coefficient for the primary airfoil

should look something like sketch 1. (The pressure distributions for the root airfoils should be qualitatively similar.)
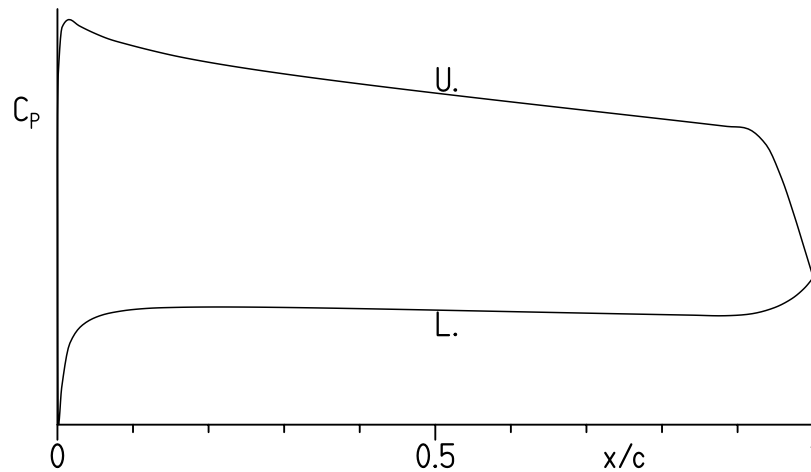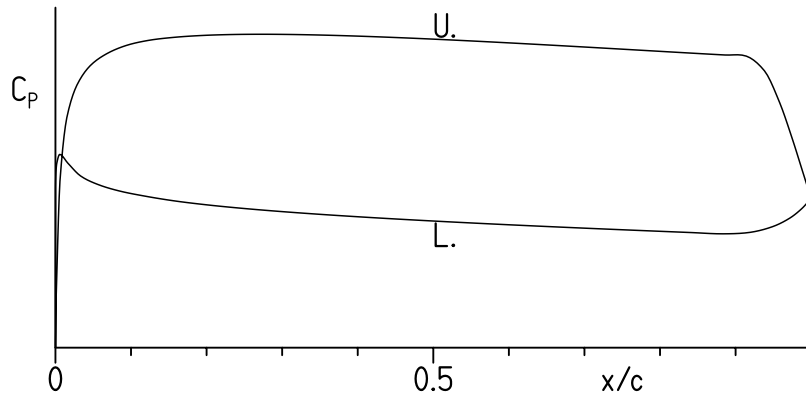

Sketch 1

To achieve a high maximum lift coefficient without significant separation, essentially the entire upper surface is used for the pressure recovery. Because the very low Reynolds number will result in laminar flow over the entire upper surface, the adverse pressure gradient must be shallow to avoid laminar separation. The steep, adverse pressure gradient aft of about 90-percent chord is a "separation ramp," originally proposed by F. X. Wortmann,[1] which confines separation to a small region near the trailing edge. By constraining the movement of the sep-aration point at high angles of attack, high lift coefficients can be achieved with little drag penalty. This feature has the added benefit of initiating docile stall characteristics. (See ref. 9.)

The amounts of pressure recovery on the upper and lower surfaces are determined by the airfoil-thickness and pitching-moment constraints and the objective of a reasonable range of lift coefficients without significant separation.

---

[1]Director, Institute for Aerodynamics and Gas Dynamics, University of Stuttgart, Germany.

The pressure distribution along the lower surface near the minimum lift coefficient should be similar in nature to that along the upper surface near the maximum lift coefficient, as illustrated in sketch 2.

Sketch 2

Execution

Given the pressure distributions previously discussed, the design of the airfoils is reduced to the inverse problem of transforming the pressure distributions into airfoil shapes. The Eppler Airfoil Design and Analysis Code (refs. 3 and 4) was used because of its unique capability for multipoint design and because of confidence gained during the design, analysis, and experimental verification of many other airfoils. (See refs. 10–12, for example.)

The primary airfoil, which corresponds to the radii outboard of that for the maximum local blade chord (i.e., $r \geq 0.17$), is designated the SE403. The root airfoils, the SE404 and SE405, were derived from the SE403 airfoil to increase the aerodynamic and geometric compatibilities of the three airfoils. The airfoil shapes are shown in figure 12 and the coordinates are contained in tables III, IV, and V. The SE403 airfoil thickness is 4.66-percent chord; the SE404, 7.01-percent chord; and the SE405, 9.32-percent chord, which satisfy the design constraints.

THEORETICAL PROCEDURE

The pressure distributions and section characteristics are predicted using the method of references 3 and 4 for Reynolds numbers of 7,000, 10,000, and 15,000. Because the free-stream Mach number for all relevant operating conditions remains below 0.2, all results are incompressible. Because of the very low Reynolds number, it is unlikely that leading-edge

roughness can force transition and, therefore, all results are computed with transition free (i.e., smooth) using a critical amplification factor of 11.

For comparison, the section characteristics of the SE403 airfoil are also predicted using the method of reference 5. The computations are performed with transition free using a critical amplification factor of 9.

RESULTS

Pressure Distributions

The inviscid pressure distributions for the SE403 airfoil at various angles of attack are shown in figure 13.

Section Characteristics

The section characteristics of the SE403 airfoil predicted using the method of references 3 and 4 are shown in figure 14, along with the separation locations. At 75-percent radius, for which the Reynolds number is approximately 12,800, the lift-to-drag ratio at a lift coefficient of 1 is about 27. Thus, the drag-to-lift ratio is about 0.036. The airfoil exhibits little separation over the range of lift coefficients from 0.75 to 1.03, which meets the design objective. (The small, trailing-edge separation predicted on the upper surface is caused by the separation ramp; see fig. 13.) The zero-lift pitching-moment coefficient is predicted to be –0.22, which exceeds the design constraint. Because of boundary-layer displacement effects not accounted for in the analysis, the pitching-moment coefficient is probably overpredicted by at least 20 percent. Therefore, the actual zero-lift pitching-moment coefficient should less negative than –0.18, which satisfies the design constraint.

The effect of Reynolds number on the section characteristics of the SE403 airfoil is summarized in figure 15. Because the flow is essentially completely laminar due to the very low Reynolds numbers, laminar rather than turbulent separation affects the lift and pitching-moment coefficients. Because laminar separation is independent of Reynolds number, the zero-lift angle of attack, the lift-curve slope, and the pitching-moment coefficient as well as the minimum and maximum lift coefficients are unaffected by Reynolds number. Only the profile-drag coefficient is affected.

Because it is unlikely that leading-edge roughness can force transition, the effect of roughness on the section characteristics is probably negligible.

The effect of Reynolds number on the section characteristics of the SE404 airfoil is summarized in figure 16. The characteristics are similar to those of the SE403 airfoil, except for the extensive separation on the lower surface. This separation becomes so massive on the lower surface of the SE405 airfoil that the predicted section characteristics are not reliable.

The section characteristics of the SE403 airfoil predicted using the method of references 3 and 4 (PROFIL05) are compared with those predicted using the method of reference 5 (MSES) in figure 14. Although the results do not agree well, for such very low Reynolds numbers, it is remarkable that they are at least similar.

INTEGRATION

The SE403 airfoil is applied to the propeller blade from the radius corresponding to the maximum local chord ($r = 0.17$) outboard to the blade tip ($r = 1.00$). The SE404 and SE405 airfoils may be applied inboard of this radius as dictated by structural requirements. The airfoils should be laid out at a given radius along the curve defined by the intersection of a line inclined at the corresponding twist angle and a cylinder having the given radius. Note that the twist angle is relative to the zero-lift angle of the airfoil, not the *x*-axis.

CONCLUDING REMARKS

The present propeller optimization theory is, in principle, based on blade-element theory. Unlike other blade-element theories, however, the velocities and pressures are not averaged over the blade-element cylinders. Instead, the blades themselves are "averaged" by distributing them into an infinite number of infinitesimal blades, which yields a vorticity surface that can be treated exactly.

The theory allows optimum propellers to be designed for given thrust coefficients and advance ratios. The local airfoil drag is considered by a specified drag-to-lift ratio of the blade sections. For the case of no drag and the thrust coefficient going to zero, the present theory yields the classical and commonly used results of Betz. A finite thrust coefficient shifts the lift of the blades toward the blade tip, which is understandable because the advance angle is lower there. For a propeller of a high-altitude balloon, the difference is not negligible. The airfoil drag has the opposite effect, which is also understandable because overcoming the blade drag requires more power as the distance from the propeller axis increases. The effects do not compensate each other, however, because they have different distributions along the radius.

The resulting propellers have a finite chord at the blade tip. This has been corrected as described in the supplement by Prandtl to Betz's paper. The modification increases the diameter of the propeller slightly but does not cause any further problems.

The shortcoming of any blade-element theory is that the induced velocities from the vortex wake onto the blades are not explicitly regarded, but they are also not completely neglected. The theory assumes only that the Bernoulli equation is valid along the streamlines of the wake until the static pressure returns to free-stream. This is not guaranteed if the wakes of the propeller blades roll up and form regions with strong vorticity and low pressure. The

assumed flow satisfies the Euler equations for all streamlines that reach free-stream static pressure before joining a low-pressure region. Therefore, the flow contains the induced velocities from these streamlines. This conclusion is corroborated by the fact that the inviscid solution from the present theory converges to the Betz solution, which is derived from an assumed form of the wake flow.

The first generalization of the present theory should contain an option for specifying section drag-to-lift ratio along the blade radius. When experimental results for the airfoil performance are available, it should be possible to evaluate the drag-to-lift ratio as a function of the local Reynolds number.

In summary, the aerodynamic design of a propeller for the trajectory control of a high-altitude, scientific balloon has been performed using theoretical methods developed especially for such applications. Optimum, nonlinear chord and twist distributions have been developed in conjunction with the design of a family of airfoils, the SE403, SE404, and SE405, for the propeller. The very low Reynolds numbers along the propeller blade fall in a range that has yet to be rigorously investigated, either experimentally or theoretically.

Because the airfoil performance is the key to the propeller performance and because current theoretical airfoil methods have not been validated for such low Reynolds numbers, it is imperative that the SE403 airfoil be experimentally verified.

ACKNOWLEDGMENTS

REFERENCES

1. Betz, A.: Schraubenpropeller mit geringstem Energieverlust. Mit einem Zusatz von L. Prandtl (Screw Propeller with Least Energy Loss. With a Supplement by L. Prandtl). Nachrichten der K. Gesellschaft der Wissenschaften zu Göttingen, Mathematisch-physikalische Klasse, 1919, pp. 193–217.

2. Larrabee, E. E.: Practical Design of Minimum Induced Loss Propellers. 790585, Soc. Automot. Eng., May 1979.

3. Eppler, Richard: Airfoil Design and Data. Springer-Verlag (Berlin), 1990.

4. Eppler, Richard: Airfoil Program System "PROFIL00." User's Guide. Richard Eppler, c.2001.

5. Drela, M.: Design and Optimization Method for Multi-Element Airfoils. AIAA Paper 93-0969, Feb. 1993.

6. Zerle, Lorenz: Aerodynamische und aeroakustische Rotorberechnung unter Anwendung frei entwickelter Nachlaufwirbelschichten und retardierter Potentiale (Aerodynamic and Aeroacoustic Rotor Calculation Using Freely Developing Wake-Vortex Sheets and Retarded Potential). Fortschritt-Berichte VDI, Reihe 7, Nr. 399, 2000. (Ph.D. Dissertation, Univ. Stuttgart, 1999)

7. McCormick, Barnes W.: Aerodynamics, Aeronautics, and Flight Mechanics. Second ed. John Wiley & Sons, Inc., 1995.

8. Eppler, R.: Strömungsmechanik. Akademische Verlagsgesellschaft (Wiesbaden), 1975.

9. Maughmer, Mark D.; and Somers, Dan M.: Design and Experimental Results for a High-Altitude, Long-Endurance Airfoil. J. Aircr., vol. 26, no. 2, Feb. 1989, pp. 148–153.

10. Somers, Dan M.: Subsonic Natural-Laminar-Flow Airfoils. Natural Laminar Flow and Laminar Flow Control, R. W. Barnwell and M. Y. Hussaini, eds., Springer-Verlag New York, Inc., 1992, pp. 143–176.

11. Eppler, Richard; and Somers, Dan M.: Low Speed Airfoil Design and Analysis. Advanced Technology Airfoil Research – Volume I, NASA CP-2045, Part 1, 1979, pp. 73–99.

12. Eppler, Richard; and Somers, Dan M.: Airfoil Design for Reynolds Numbers Between 50,000 and 500,000. Proceedings of the Conference on Low Reynolds Number Airfoil Aerodynamics, UNDAS-CP-77B123, Univ. of Notre Dame, June 1985, pp. 1–14.

TABLE I.- PROPELLER OPERATIONAL SPECIFICATIONS

Parameter	Value
Propeller radius	$\leq$ 5.334 m (17.50 ft)
Shaft power P	< 500 W
Forward velocity V_∞	1.29 m/s (4.22 ft/s)
Thrust (at forward velocity) T	$\geq$ 22.7 N (5.10 lbf)
Altitude	36,576 m (120,000 ft)
Air density ρ	6.6486×10^{-3} kg/m^3 (1.2900×10^{-5} slug/ft^3)
Viscosity	1.5516×10^{-5} N·s/m^2 (3.2406×10^{-7} lbf·s/ft^2)
Speed of sound	311.1 m/s (1021 ft/s)
Pressure	459.7 Pa (9.601 lbf/ft^2)
Temperature	240.9 K (433.6° R)
Effective gravitational acceleration	9.696 m/s^2 (31.81 ft/s^2)

TABLE II.- AIRFOIL DESIGN SPECIFICATIONS

Parameter	Objective/ Constraint	Reynolds Number R	Mach Number M
Lift-to-drag ratio c_l/c_d	As high as possible		
Range of lift coefficients without significant separation	0.2	10,000	0
Zero-lift pitching-moment coefficient $c_{m,0}$	≥ -0.20		
Airfoil thickness t/c	$\geq 3\%$		

TABLE III.- SE403 AIRFOIL COORDINATES

Upper Surface		Lower Surface	
x/c	*y/c*	*x/c*	*y/c*
0.000002	0.000090	0.000021	−0.000292
.000172	.001009	.000059	−.000459
.001019	.002848	.000121	−.000603
.005958	.008441	.000219	−.000728
.015025	.014890	.000273	−.000781
.028398	.021831	.000354	−.000849
.045973	.028997	.000710	−.001082
.067685	.036173	.001726	−.001508
.093345	.043172	.005559	−.002267
.122764	.049803	.016464	−.002433
.155726	.055925	.033284	−.001225
.191944	.061431	.055861	.001035
.231097	.066219	.084072	.004153
.272832	.070203	.117577	.007908
.316767	.073317	.156077	.012137
.362498	.075516	.199147	.016599
.409595	.076773	.246279	.021092
.457613	.077081	.296907	.025429
.506090	.076451	.350413	.029432
.554557	.074911	.406133	.032935
.602537	.072506	.463362	.035787
.649556	.069293	.521357	.037854
.695143	.065343	.579351	.039026
.738838	.060735	.636560	.039221
.780197	.055558	.692188	.038388
.818795	.049904	.745444	.036510
.854235	.043866	.795552	.033608
.886143	.037528	.841757	.029739
.914172	.030933	.883339	.024971
.938138	.023896	.919462	.019319
.958469	.016557	.949091	.013290
.975344	.009714	.971783	.007783
.988447	.004295	.987622	.003523
.996991	.001014	.996930	.000892
1.000000	.000000	1.000000	.000000

TABLE IV.- SE404 AIRFOIL COORDINATES

Upper Surface		Lower Surface	
x/c	y/c	x/c	y/c
0.000018	0.000320	0.000008	−0.000197
.000278	.001495	.000099	−.000645
.000499	.002093	.000324	−.001054
.004860	.008157	.000680	−.001467
.013552	.015150	.001177	−.001914
.026667	.022656	.001697	−.002301
.044065	.030383	.008105	−.005147
.065663	.038103	.020239	−.007704
.091261	.045617	.037628	−.009399
.120661	.052729	.060001	−.010236
.153641	.059294	.087149	−.010136
.189909	.065200	.118764	−.008901
.229139	.070340	.154932	−.006448
.270972	.074625	.195443	−.003028
.315023	.077987	.239965	.001167
.360884	.080379	.288102	.005929
.408121	.081772	.339392	.011021
.456284	.082159	.393303	.016182
.504909	.081550	.449231	.021141
.553522	.079975	.506505	.025623
.601644	.077479	.564387	.029364
.648797	.074121	.622083	.032127
.694506	.069973	.678750	.033711
.738309	.065120	.733514	.033968
.779758	.059652	.785485	.032811
.818426	.053665	.833771	.030218
.853912	.047257	.877499	.026206
.885838	.040514	.915637	.020754
.913850	.033481	.946887	.014484
.937764	.025949	.970698	.008546
.958064	.018048	.987202	.003878
.974982	.010628	.996837	.000982
.988213	.004714	1.000000	.000000
.996915	.001115		
1.000000	.000000		

TABLE V.- SE405 AIRFOIL COORDINATES

Upper Surface		Lower Surface	
x/c	*y/c*	*x/c*	*y/c*
0.000003	0.000137	0.000035	−0.000487
.000084	.000816	.000209	−.001091
.000513	.002292	.000510	−.001717
.003668	.007390	.001409	−.003020
.011900	.014966	.002638	−.004348
.024710	.023076	.010760	−.009901
.041905	.031397	.023554	−.015171
.063375	.039688	.040919	−.019836
.088906	.047743	.062544	−.023648
.118289	.055358	.088177	−.026292
.151294	.062384	.117577	−.027182
.187623	.068705	.151261	−.026072
.226942	.074209	.189190	−.023287
.268890	.078807	.231172	−.019027
.313077	.082427	.276953	−.013532
.359088	.085020	.326206	−.007100
.406486	.086556	.378515	−.000080
.454817	.087028	.433369	.007139
.503613	.086447	.490156	.014145
.552395	.084842	.548164	.020524
.600682	.082259	.606583	.025885
.647991	.078761	.664519	.029881
.693844	.074423	.721008	.032233
.737775	.069330	.775039	.032748
.779334	.063579	.825577	.031327
.818089	.057269	.871589	.027946
.853636	.050502	.911837	.022552
.885595	.043370	.944748	.015900
.913603	.035916	.969674	.009420
.937472	.027914	.986818	.004274
.957738	.019482	.996754	.001079
.974682	.011518	1.000000	.000000
.988014	.005128		
.996849	.001216		
1.000000	.000000		
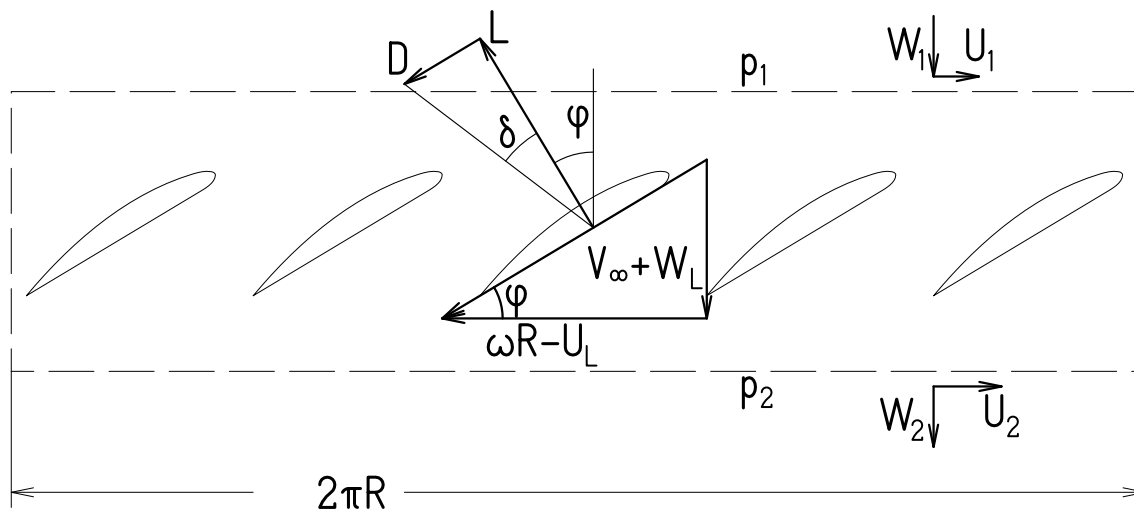
Figure 1.- Fundamental parameters of blade-element theory of propellers.

$$W_1 \downarrow \quad U_1 \qquad p_1$$

$$\gamma \qquad \downarrow V_\infty + W$$

$$W_2 \downarrow \quad U_2 \qquad p_2 \qquad V_\infty + W \qquad U = \gamma \qquad \omega R$$
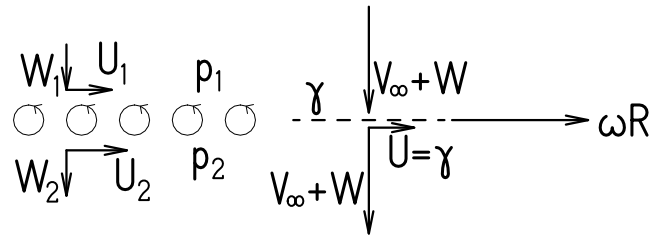
Figure 2.- Vorticity surface for infinite number of propeller blades.
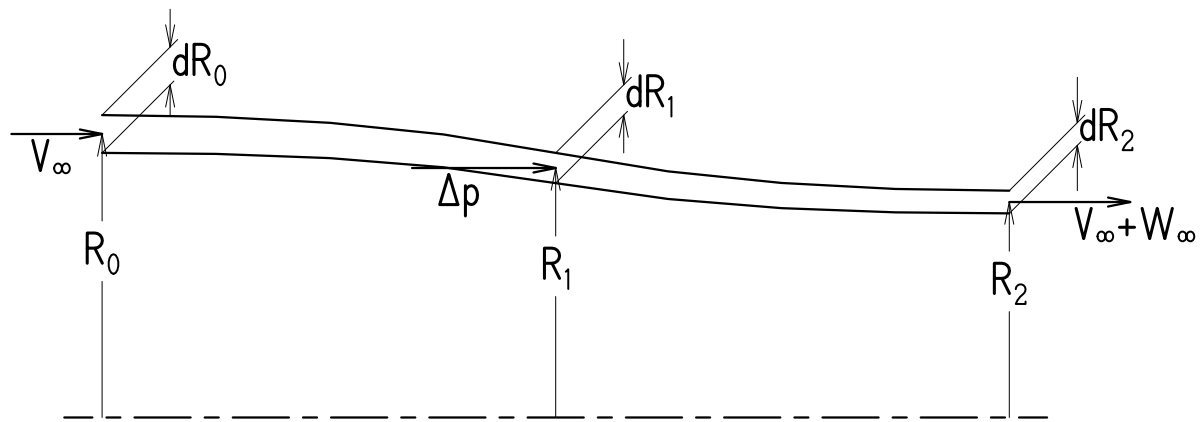
Figure 3.- Cross section of flow tube.
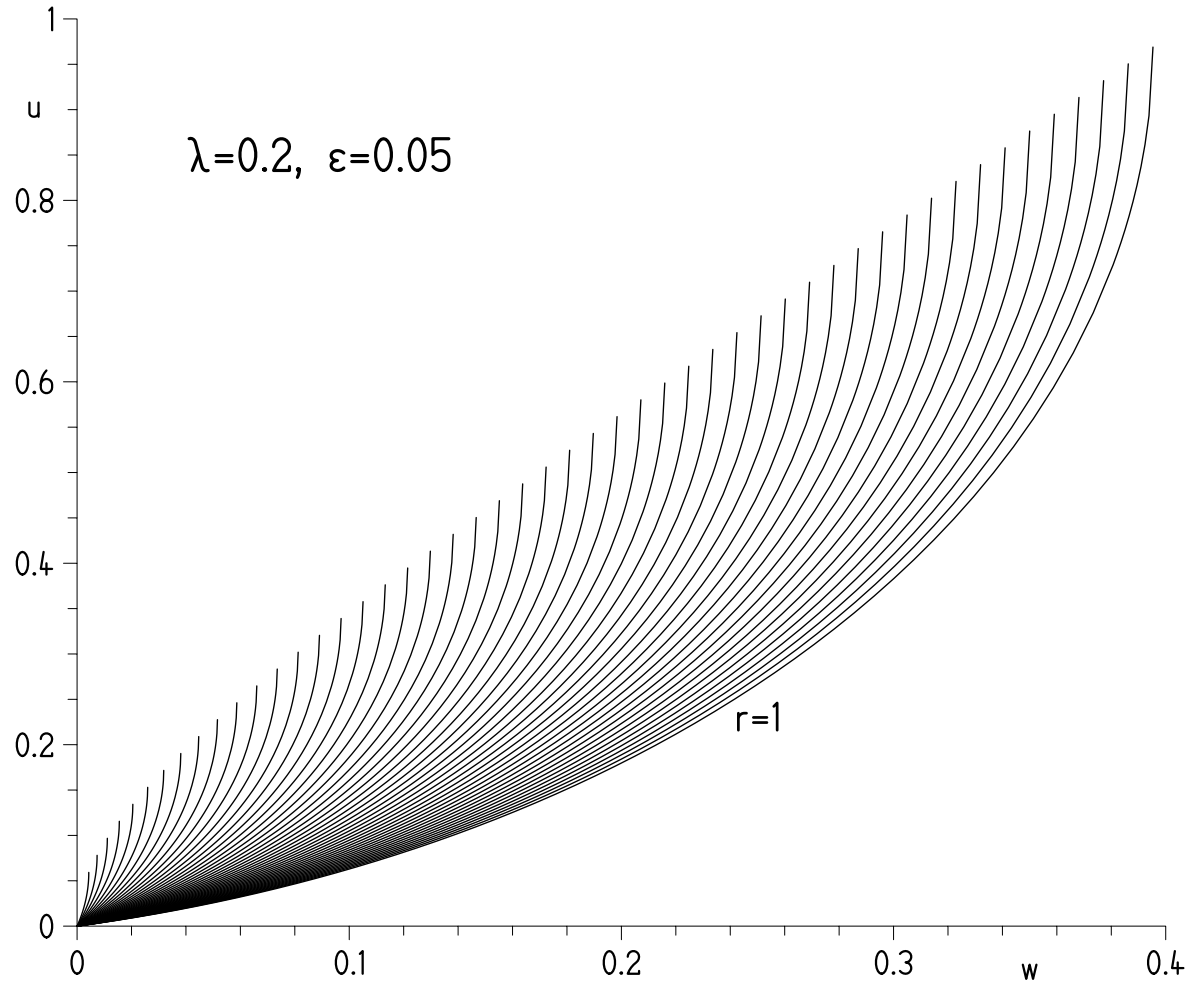
Figure 4.- Ellipses from equation (15) for $\lambda = 0.2$ and $\varepsilon = 0.05$.
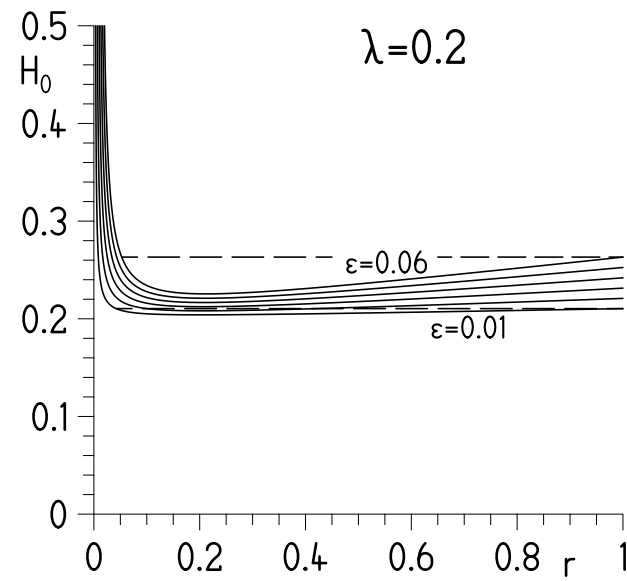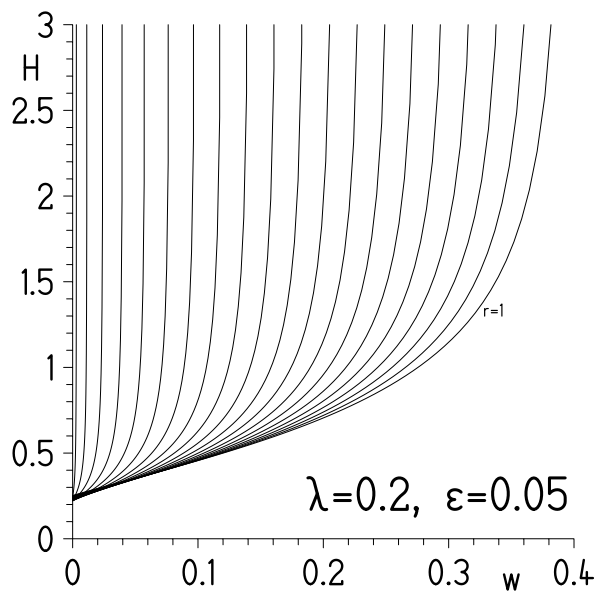
Figure 5.- Function $H(w)$ for $\lambda = 0.2$ and $\varepsilon = 0.05$ and a series of equidistant r values; function $H_0(r)$ for $\lambda = 0.2$ and six ε values.
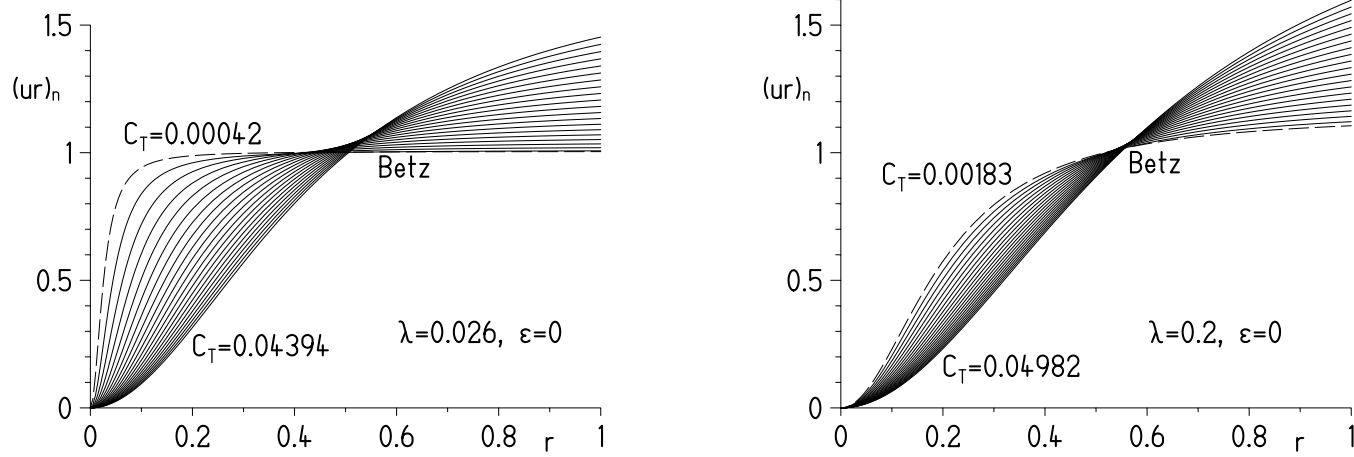
Figure 6.- Normalized functions $(ur)_n$ of optimum propellers for $\lambda = 0.026$ and $\lambda = 0.2$, with $\varepsilon = 0$; broken lines represent Betz solution (ref. 1).
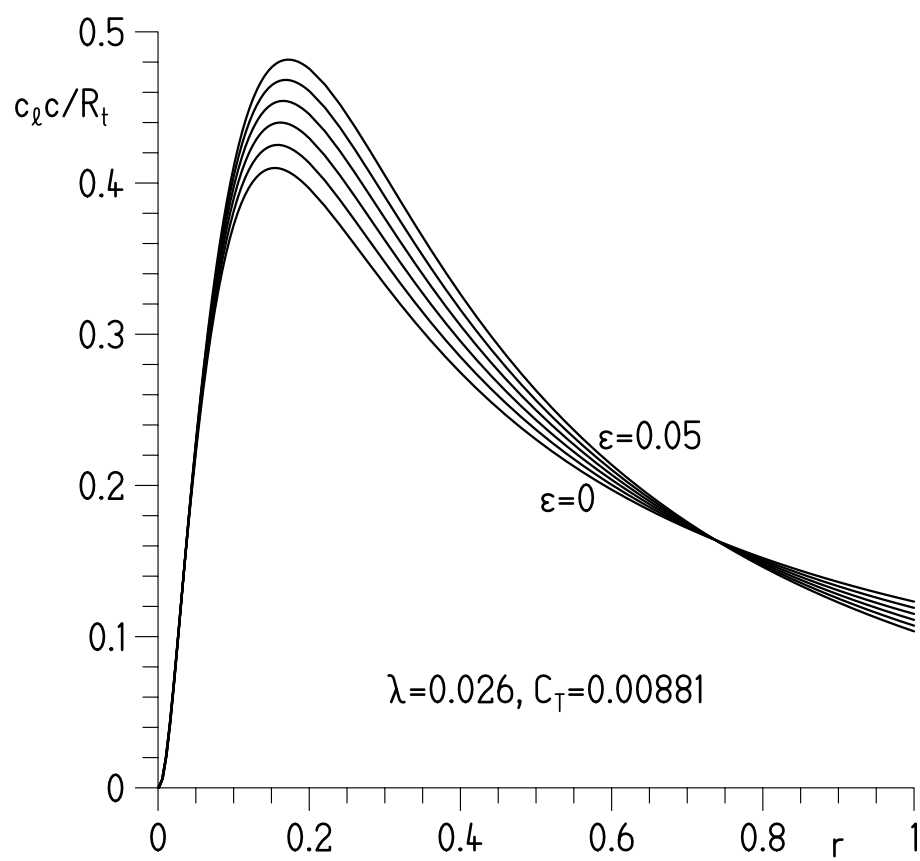
Figure 7.- Effect of drag-to-lift ratio on lift-chord distribution of high-altitude propeller.
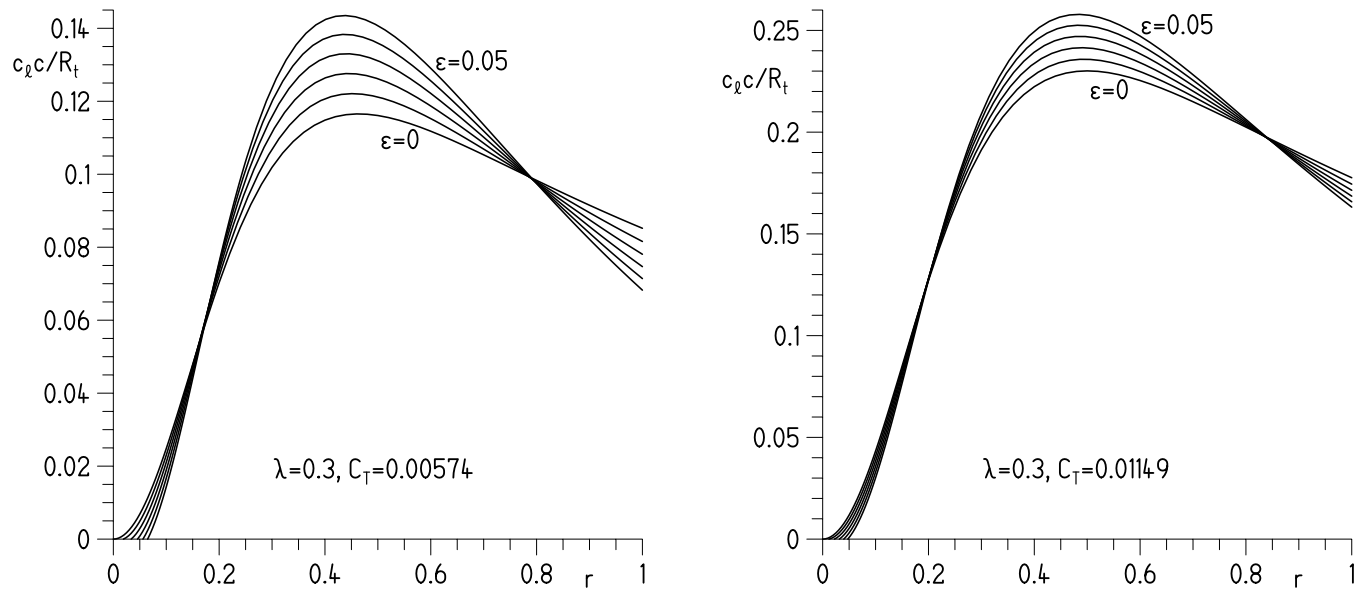
Figure 8.- Effect of drag-to-lift ratio on lift-chord distributions of optimum propellers with higher nondimensional forward velocity and different thrust coefficients.

$R_t=5m$ $U_t=50m/s$ $\varepsilon=0.04$ $R_{max}=13466$ $P=161.4W$

Legend:
- $c_\ell c/R_t$
- R/R_{max}
- $\varphi/100$ (deg.)
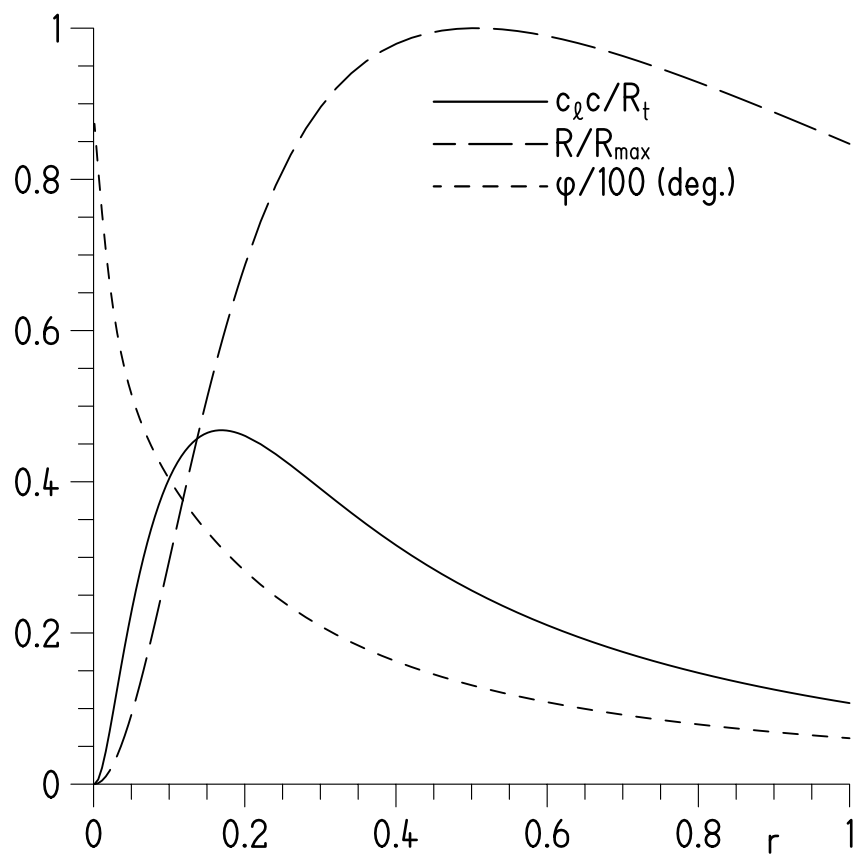
(a) $U_t = 50$ m/s.

Figure 9.- Optimum propellers for high-altitude balloon.

R_t=5m U_t=75m/s ε=0.05 R_{max}=10258 P=184.5W

Legend:
— $c_\ell c/R_t$
– – – R/R_{max}
- - - φ/100 (deg.)
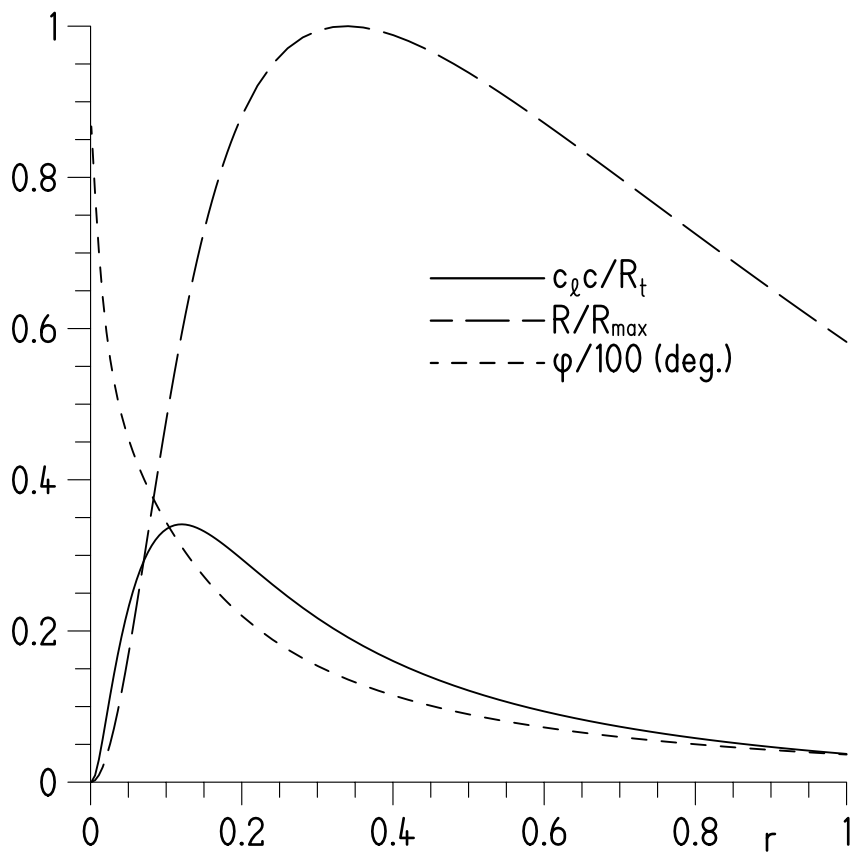
(b) $U_t = 75$ m/s.

Figure 9.- Continued.

$R_t=5m \ U_t=100m/s \ \varepsilon=0.06 \ R_{max}=9432 \ P=214.8W$

Legend:
$c_{\ell}c/R_t$
R/R_{max}
$\varphi/100 \ (deg.)$
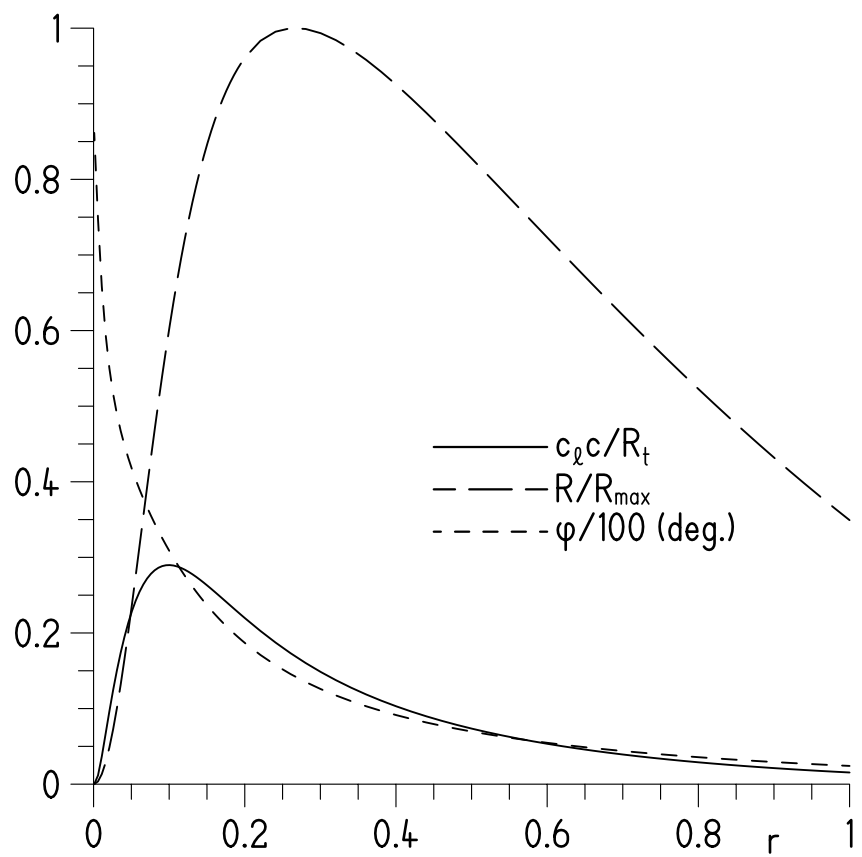
(c) $U_t = 100$ m/s.

Figure 9.- Concluded.
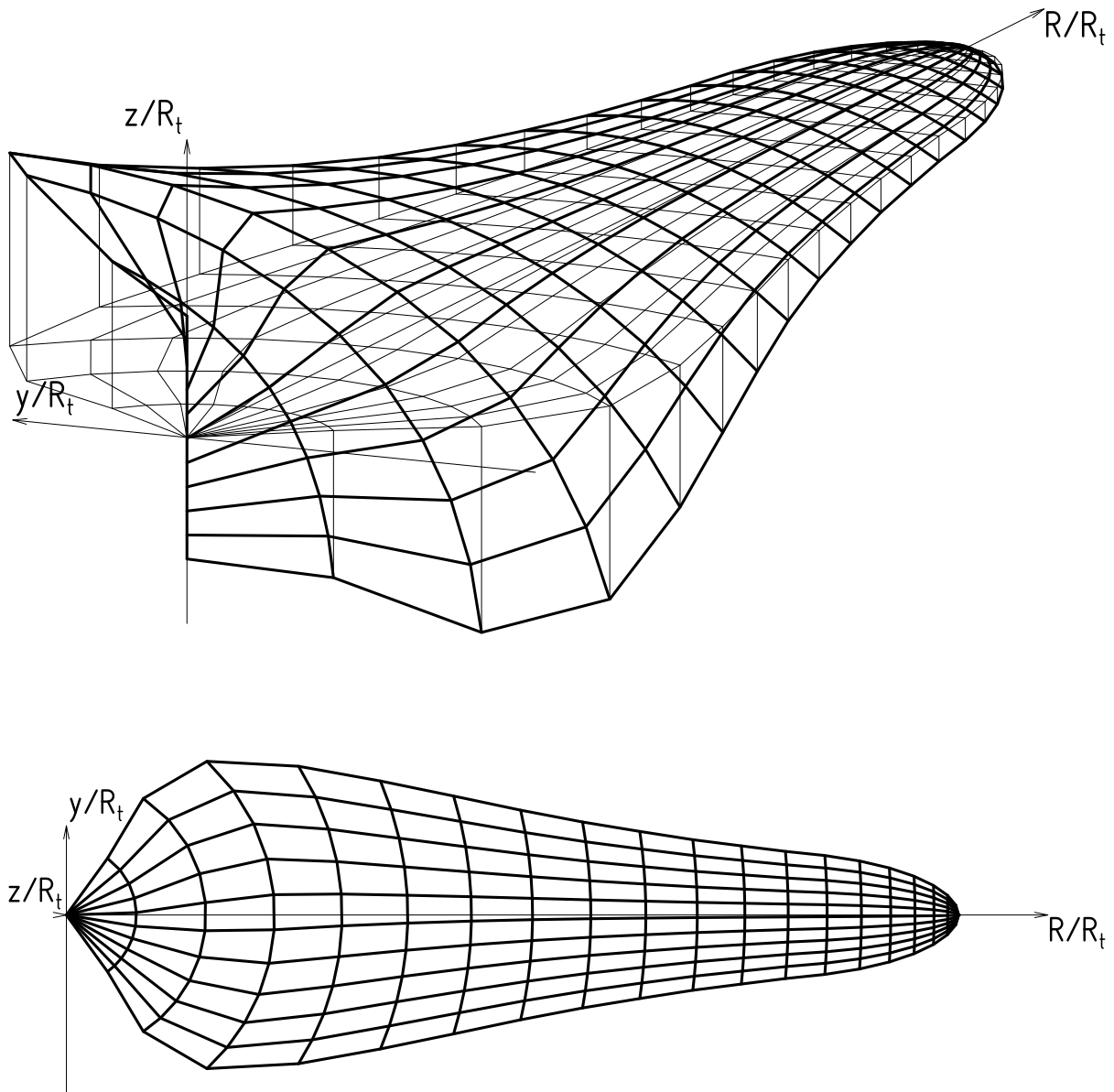
Figure 10.- Axonometric projection and plan view of optimum propeller for high-altitude balloon.
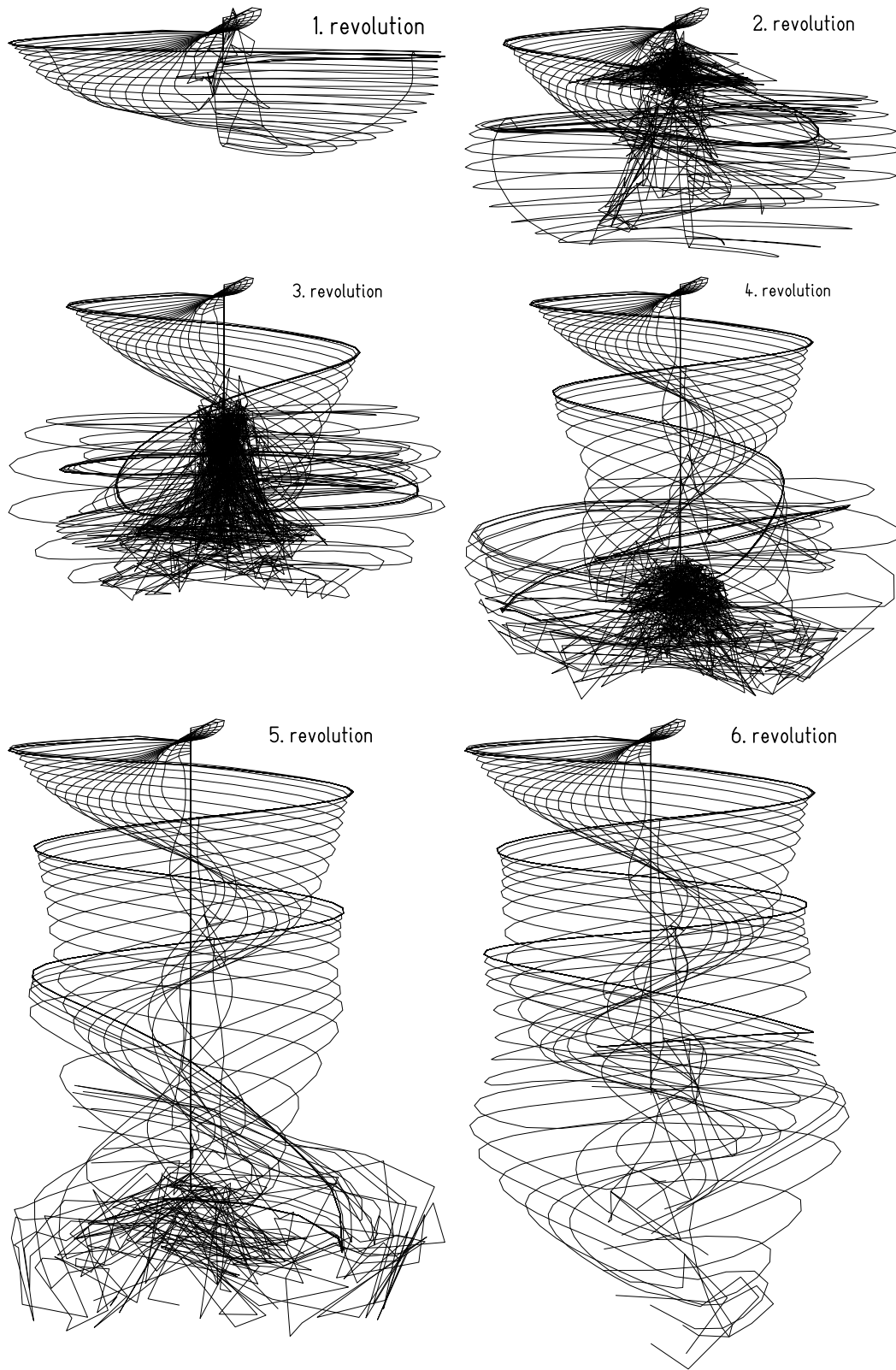
Figure 11.- Development of free vortex wake of optimum propeller for high-altitude balloon.

SE403 4.66%
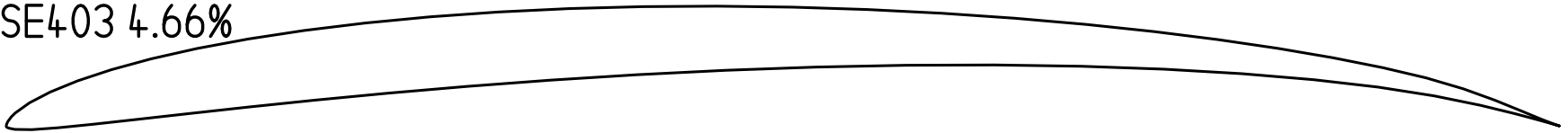
SE404 7.01%
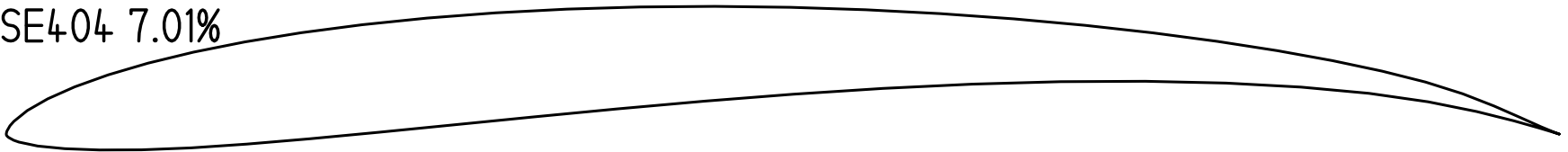
SE405 9.32%

Figure 12.- Airfoil shapes.
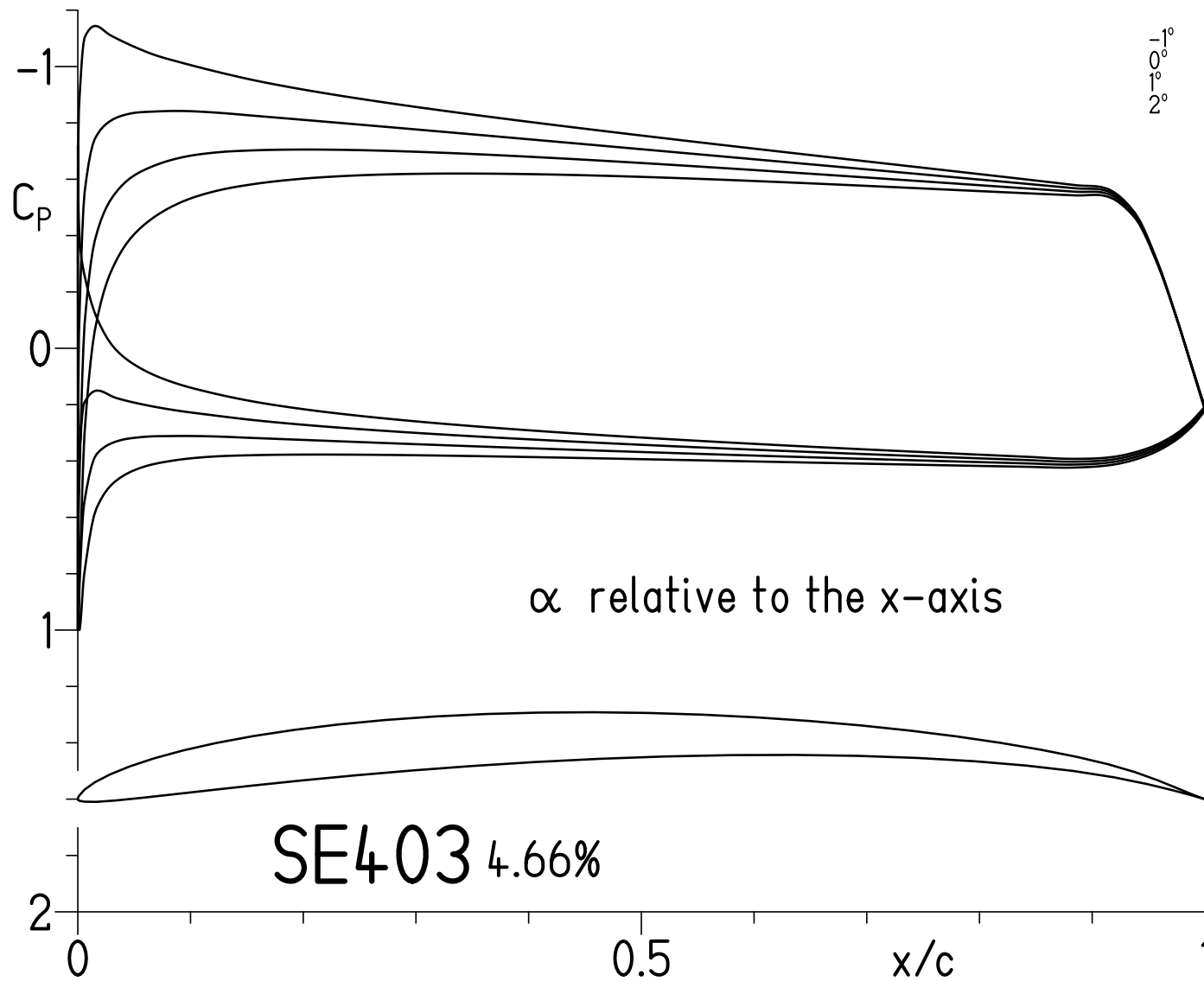
Figure 13.- Inviscid pressure distributions for SE403 airfoil.

SE403 R = 7,000
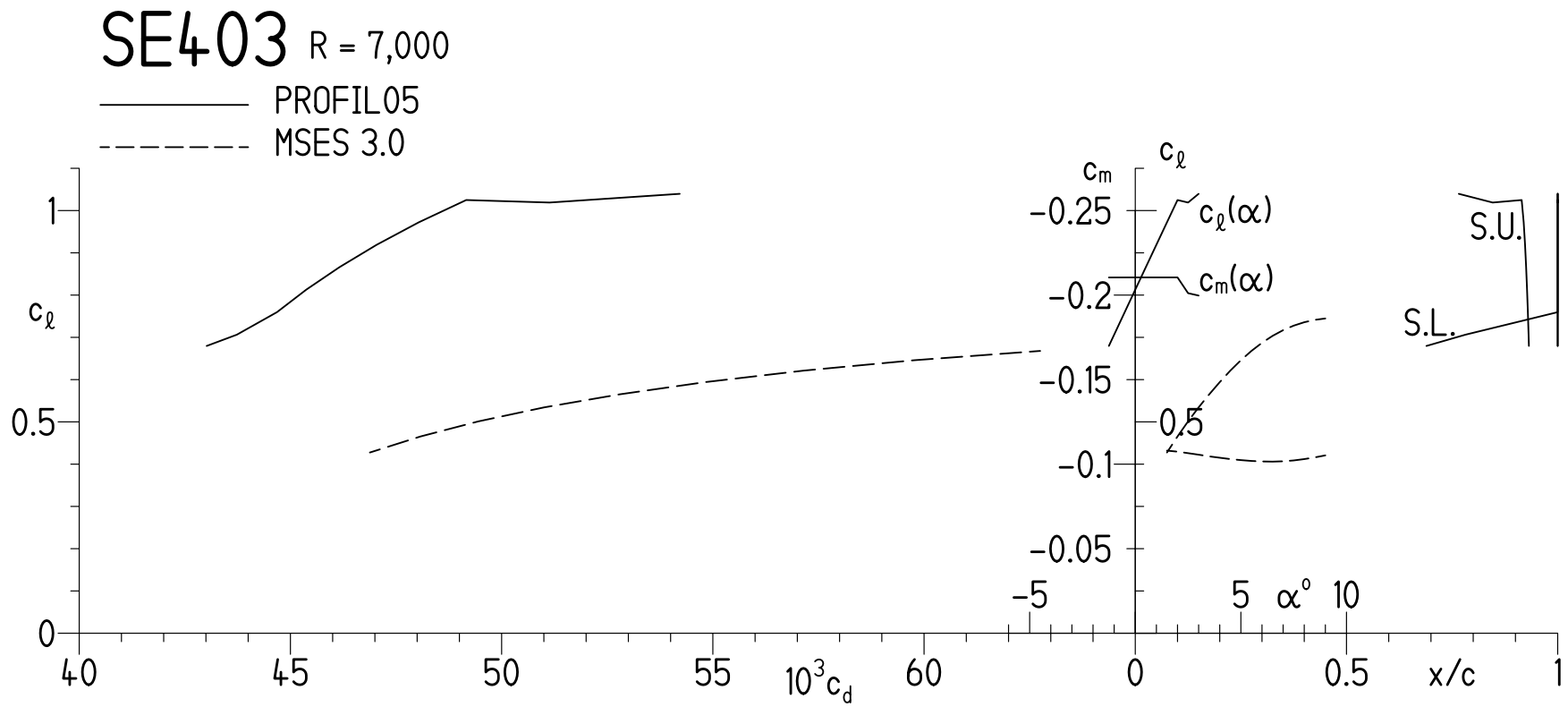
———— PROFIL05
– – – – MSES 3.0

(a) *R* = 7,000.

Figure 14.- Section characteristics of SE403 airfoil.

SE403 R = 10,000

PROFIL05
MSES 3.0
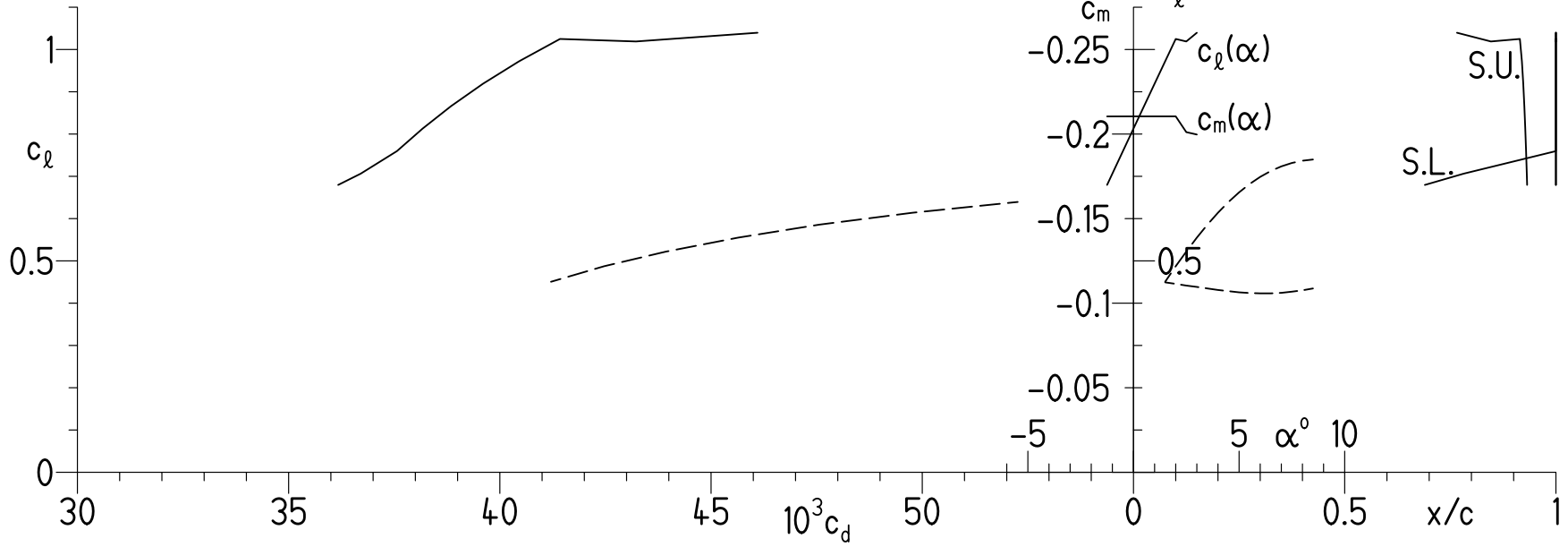
(b) $R = 10,000$.

Figure 14.- Continued.

SE403 R = 15,000

PROFIL05
MSES 3.0
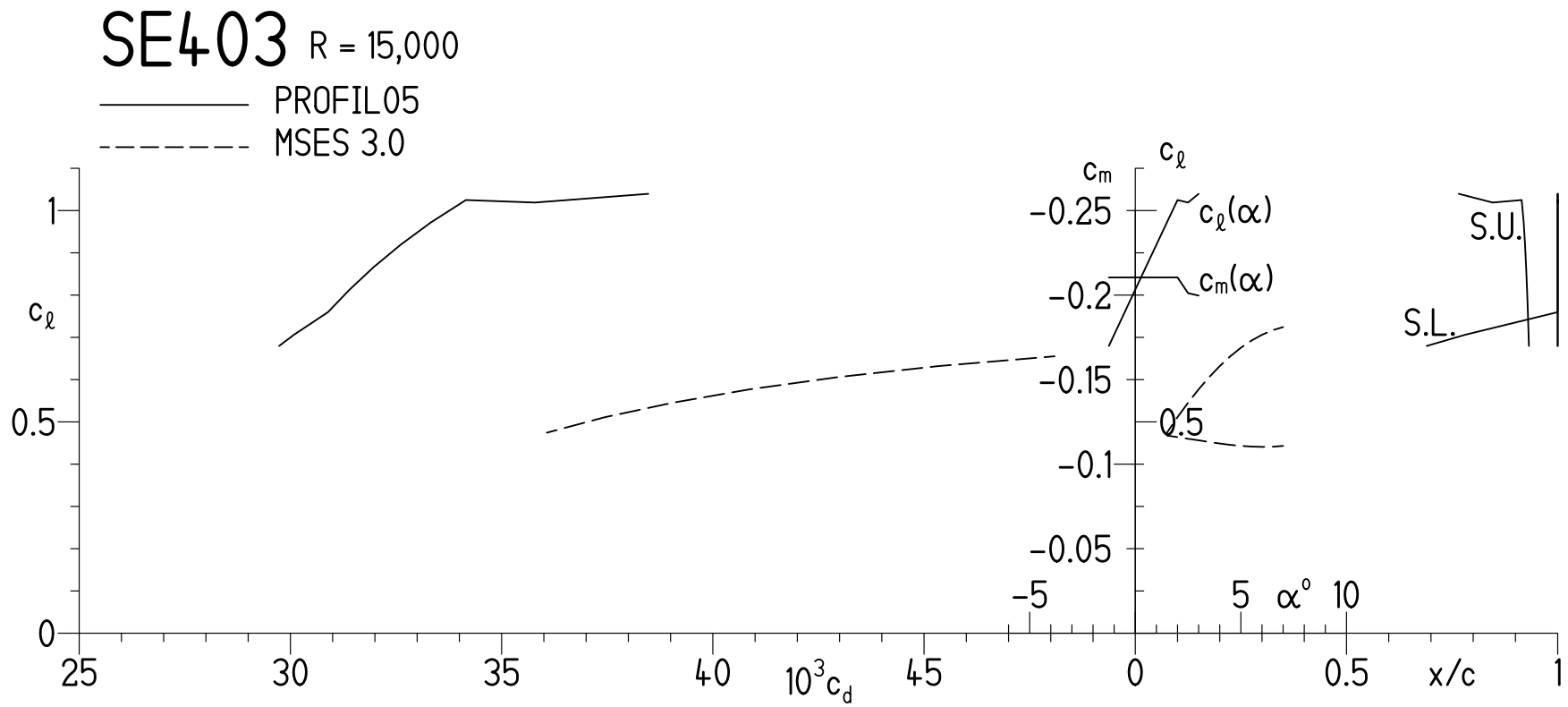
(c) *R* = 15,000.

Figure 14.- Concluded.
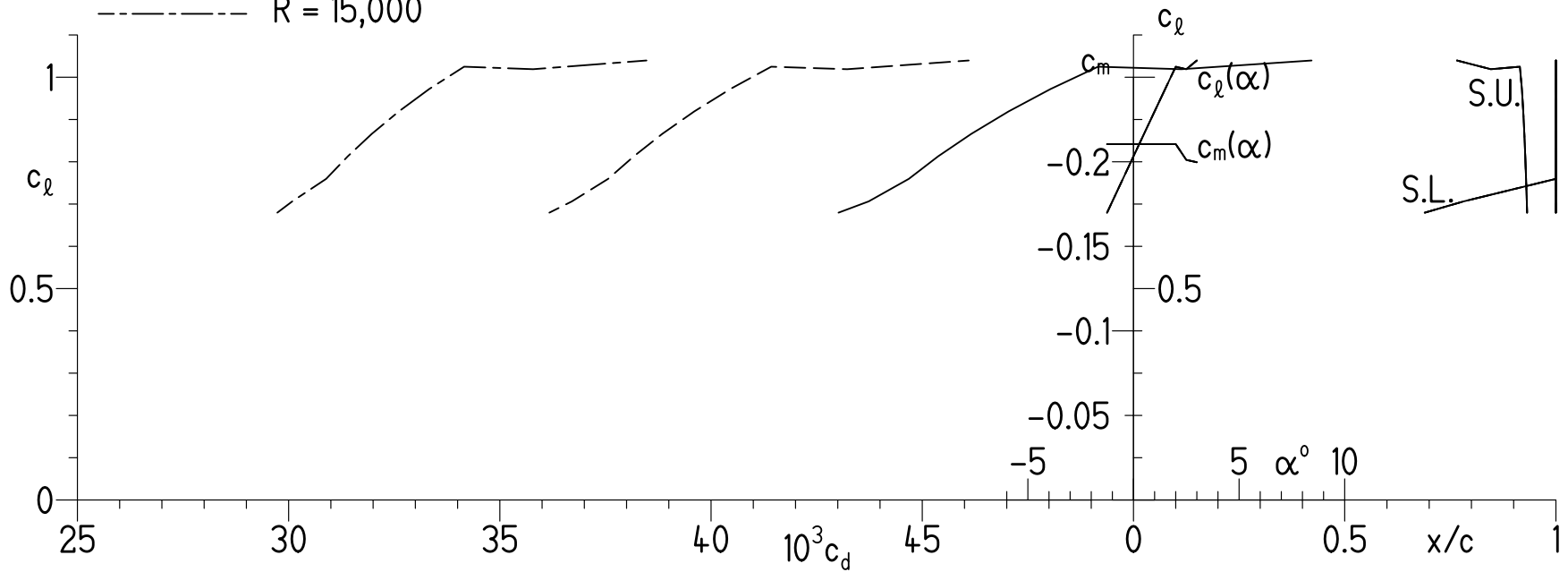
Figure 15.- Effect of Reynolds number on section characteristics of SE403 airfoil.
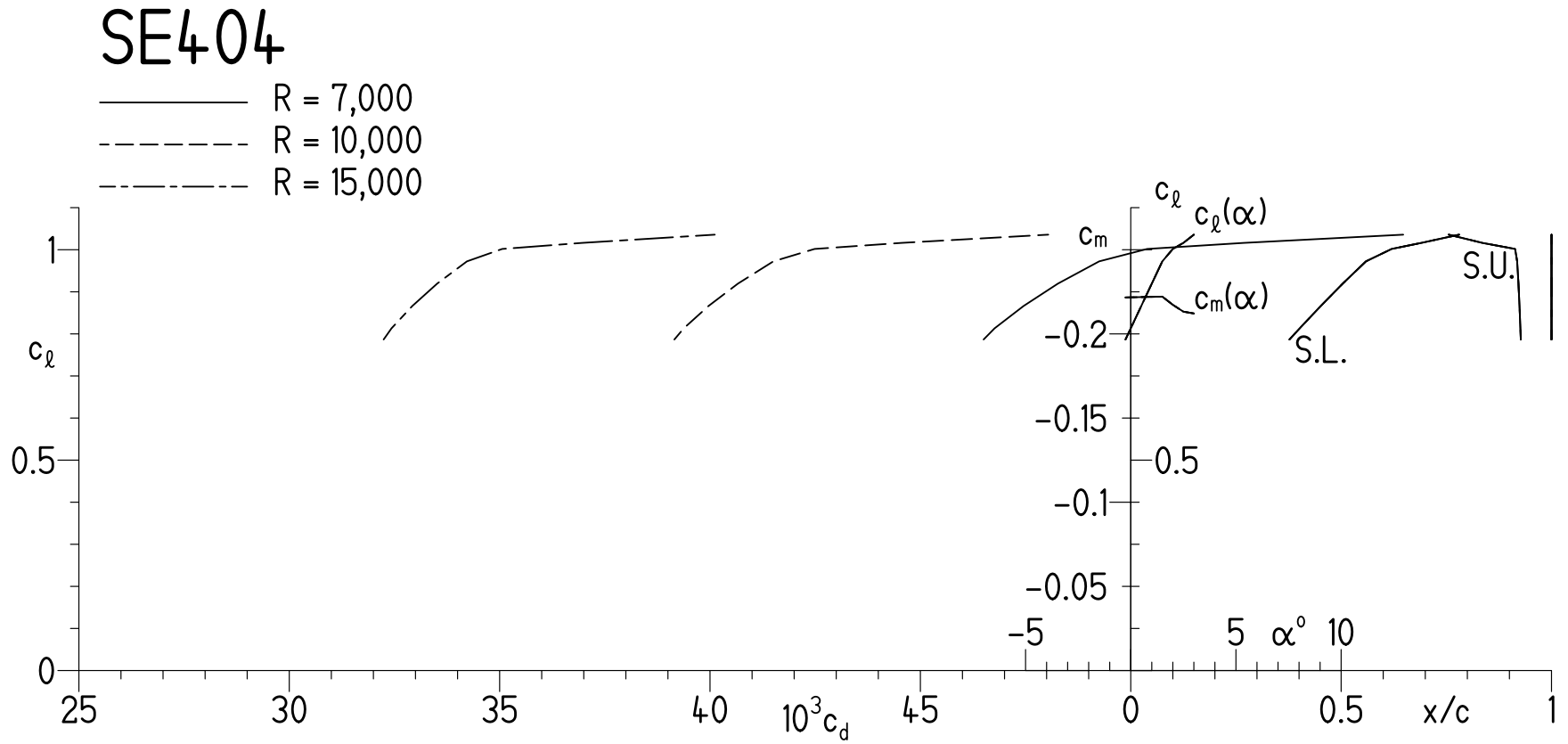
SE404

Figure 16.- Effect of Reynolds number on section characteristics of SE404 airfoil.

REPORT DOCUMENTATION PAGE

1. REPORT DATE (DD-MM-YYYY)	2. REPORT TYPE	3. DATES COVERED (From - To)
03-01-2012	Contractor Report	14 December 2004 to 31 December 2005.

4. TITLE AND SUBTITLE

AERODYNAMIC DESIGN OF A PROPELLER FOR HIGH-ALTITUDE BALLOON TRAJECTORY CONTROL

5a. CONTRACT NUMBER

5b. GRANT NUMBER
NNG05WC00G

5c. PROGRAM ELEMENT NUMBER

6. AUTHOR(S)

Eppler, Richard and Somers, Dan M.

5d. PROJECT NUMBER

5e. TASK NUMBER

5f. WORK UNIT NUMBER

7. PERFORMING ORGANIZATION NAME(S) AND ADDRESS(ES)

Wallops Flight Facility, Wallops Island, VA 23337
Airfoils, Incorporated
122 Rose Drive
Port Matilda, PA 16870-7535

8. PERFORMING ORGANIZATION REPORT NUMBER

9. SPONSORING/MONITORING AGENCY NAME(S) AND ADDRESS(ES)

National Aeronautics and Space Administration
Washington, DC 20546-0001

10. SPONSORING/MONITOR'S ACRONYM(S)

NASA

11. SPONSORING/MONITORING REPORT NUMBER
CR-2012-215893

12. DISTRIBUTION/AVAILABILITY STATEMENT

Unclassified-Unlimited, Subject Category: 02
Report available from the NASA Center for Aerospace Information, 7115 Standard Drive, Hanover, MD 21076. (443)757-5802

13. SUPPLEMENTARY NOTES

14. ABSTRACT
The aerodynamic design of a propeller for the trajectory control of a high-altitude, scientific balloon has been performed using theoretical methods developed especially for such applications. The methods are described. Optimum, nonlinear chord and twist distributions have been developed in conjunction with the design of a family of airfoils, the SE403, SE404, and SE405, for the propeller. The very low Reynolds numbers along the propeller blade fall in a range that has yet to be rigorously investigated, either experimentally or theoretically.

15. SUBJECT TERMS

Propeller; SE403, SE404, SE405; airfoils; low speed; laminar flow; low Reynolds number

16. SECURITY CLASSIFICATION OF:

a. REPORT	b. ABSTRACT	c. THIS PAGE
Unclassified	Unclassified	Unclassified

17. LIMITATION OF ABSTRACT
Unclassified

18. NUMBER OF PAGES
51

19b. NAME OF RESPONSIBLE PERSON
Magdi Said

19b. TELEPHONE NUMBER (Include area code)
(757) 824-1386